Central Pyrenees Mountain Building: Constraints From New LT Thermochronological Data From the Axial Zone

Maxime Waldner, Nicolas Bellahsen, Frederic Mouthereau, Matthias Bernet, Raphael Pik, Claudio L. Rosenberg, Melanie Balvay

AGU ADVANCING EARTH AND SPACE SCIENCE

Tectonics

RESEARCH ARTICLE
10.1029/2020TC006614

Key Points:

- Early mid-Cretaceous cooling suggests a significant denudation of the Axial Zone during rifting
- Slow orogenic cooling (5–10°C/Myrs) from 70 to 40 Ma suggest significant distributed shortening (~ 15 km) during this period
- Acceleration of cooling/exhumation (over 30 C/Myrs, 800 m/Myrs) around 40 Ma in the Maladeta massif is coeval with the Rialp ramp activation

Supporting Information:

- Supporting Information S1
- Data Set S1

Correspondence to:
M. Waldner,
maxime.waldner@gmail.com

Citation:
Waldner, M., Bellahsen, N., Mouthereau, F., Bernet, M., Pik, R., Rosenberg, C. L., & Balvay, M. (2021). Central Pyrenees mountain building: Constraints from new LT thermochronological data from the Axial Zone. *Tectonics*, *40*, e2020TC006614. https://doi.org/10.1029/2020TC006614

Received 7 NOV 2020
Accepted 2 FEB 2021

Central Pyrenees Mountain Building: Constraints From New LT Thermochronological Data From the Axial Zone

Maxime Waldner[1], Nicolas Bellahsen[1], Frederic Mouthereau[2], Matthias Bernet[3], Raphael Pik[4], Claudio L. Rosenberg[1], and Melanie Balvay[3]

[1]Sorbonne Université, CNRS-INSU, Institut des Sciences de la Terre Paris, Paris, France, [2]Géosciences Environnement Toulouse, Université de Toulouse, CNRS, IRD, UPS, CNES, Toulouse, France, [3]ISTerre, Université Grenoble Alpes, CNRS, IRD, Grenoble, France, [4]CRPG, UMR 7358 CNRS-Université de Lorraine, BP20, Vandoeuvre-lès-Nancy, France

Abstract Early phases of mountain building are usually poorly constrained although they may provide insights into both the wedge rheology and the role of inheritance. In the central Pyrenean Axial Zone, a main exhumation peak at 35–30 Ma is particularly well constrained but the previous exhumation stages are much less constrained. In this study, we present new low-temperature thermochronological zircon fission-track and (U-Th)/He data and structural observations to constrain the thermal history of the Axial Zone and its shortening sequence during the whole Alpine collision. The dataset collected along the ECORS profile suggests two main collisional cooling phases. An early stage of Alpine shortening (from 70 to 40 Ma) is characterized by low rates of cooling/exhumation in the whole Axial Zone around 5–10°C/Myr and 200 ± 50 m/Myr. During this phase, deformation was distributed within the whole Axial Zone. This result questions the occurrence of a quiescence phase in the Axial Zone. Between 40 and 20 Ma, a more localized second phase with cooling rates around 30°C/Myr and high exhumation rates >800 m/Myr is only recorded in the Maladeta massif. During this second phase, much lower denudation rates are recorded further north and south, thus suggesting rather symmetrical exhumation in the Axial Zone, controlled by underplating of the youngest crustal ramp, the Rialp thrust. This sequence of shortening, from distributed to localized deformation, appears to be characteristic in other collisional wedges as well.

1. Introduction

The Pyrenean mountain belt (Figure 1a) is an asymmetrical Alpine doubly-vergent collisional wedge (Beaumont et al., 2000; Choukroune & the ECORS-Pyrenees Team, 1989; Mouthereau et al., 2014; Muñoz, 1992; Roure et al., 1989; Seguret, 1972; Teixell, 1996; Vergés et al., 1995) linked to the closure of an Early Cretaceous hyper-thinned rift system (Figure 1; Lagabrielle et al., 2010; Olivet, 1996; Vielzeuf & Kornprobst, 1984) between European and Iberian plates. Rifting started during Triassic times, lasted during Jurassic and Early Cretaceous times, and involved strike-slip deformation (Olivet, 1996; Srivastava et al., 1990; Tugend et al., 2015). Convergence started at around 83 Ma (Olivet, 1996), only few Myrs after crustal thinning and mantle exhumation, which took place at around 110–90 Ma (Clerc & Lagabrielle, 2014; de Saint Blanquat et al., 2016; Golberg & Leyreloup, 1990; Lagabrielle et al., 2010; Masini et al., 2014; Vacherat et al., 2016). Such an event may have had a profound thermal effect on later shortening in the North Pyrenean Zone (NPZ; Vacherat et al., 2014, 2016; Ternois et al., 2019) and possibly in the Axial Zone (AZ) (Bellahsen et al., 2019). Moreover, rifting post-dated the Variscan orogeny which strongly deformed rocks currently outcropping in the AZ.

Alpine shortening started in the NPZ with the closure of the Pyrenean rift and subsequently propagated to the AZ and the external zones. In the Meso-Cenozoic basins of the South Pyrenean Zone (SPZ; Figures 1a and 1b), the timing and amount of shortening of each major structure are well defined and thus provide constraints for the AZ structural evolution: the classical interpretation of the ECORS (Etude Continentale et Océanique par Réflexion et Réfraction Sismique) deep reflection profile suggests the development of an antiformal stack in the AZ (e.g., Muñoz, 1992; Mouthereau et al., 2014; Roure et al., 1989). The structure of the deepest part of the crustal root of the orogen is now well constrained by recent tomographic images (Chevrot et al., 2014, 2015, 2018). These contributions quantified the Alpine component of shortening throughout the mountain belt between 71 and 111 km (Erdős et al., 2014; Espurt et al., 2019; Grool et al., 2018; Mouthereau et al., 2014; Teixell et al., 2018;). In the AZ, around 20 km of shortening are accommodated

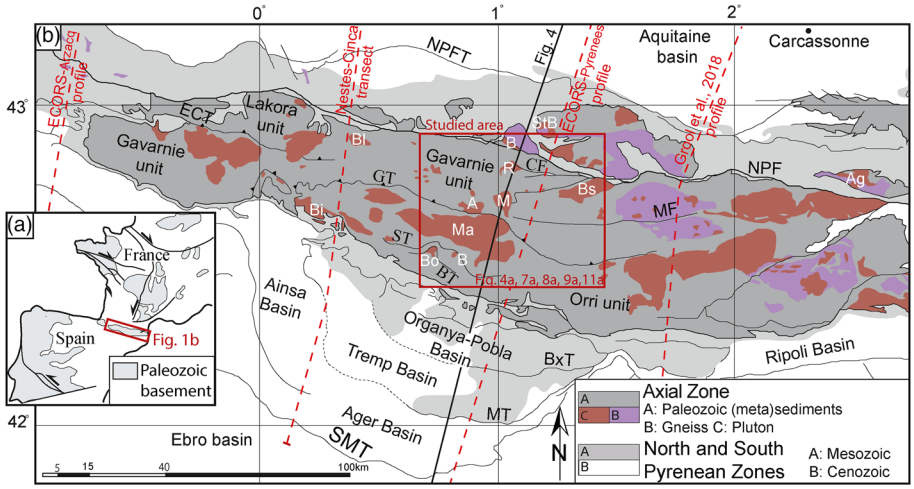

Figure 1. (a) Simplified structural map including main structures, Mesozoic basins and Paleozoic outcrops; (b) structural map of the Pyrenees presenting major tectonic structures (units, thrusts), plutonic massifs, metamorphic domes, and main southern basins. NPFT: North Pyrenean Frontal thrust; NPF: North Pyrenean Fault; ECT: Eaux-Chaudes thrust; GT: Gavarnie thrust; CF: Couflens Fault; MF: Merens Fault; BT: Bono thrust; BxT: Boixols thrust; MT: Montsec thrust; SMT: Sierra Marginales thrust; A: Arties; Ag: Agly; B: Bethmale; Bi: Bielsa; Bl: Bordere-Lourons; Bo: Bono; Br: Barruera; Bs: Bassies; C: Castillon; E: Erill; M: Marimanya; Ma: Maladeta; R: Riberot; StB: Saint Barthélemy.

by the Gavarnie thrust (Figure 1; Mouthereau et al., 2014) which is responsible for the burial of the Maladeta Massif according to multi-diffusion domains (MDD) thermal modeling of feldspar $^{39}Ar/^{40}Ar$ (Metcalf et al., 2009). However, a recent study (Cochelin et al., 2018) proposed a structural restoration which shows a very small amount of Alpine shortening in the AZ, arguing for mainly Variscan deformation. This study argues for a limited tilting of the tectonic units in the northern AZ, and therefore suggests that the "classic" antiformal stack model must be refined. However, the latter restoration does not take into account the tectonic sequence documented by thermochronological studies, which clearly emphasizes the Alpine, thrust-related exhumation since at least 50 Ma (Figure 2; e.g., Fitzgerald et al., 1999; Espurt et al., 2019; Mouthereau et al., 2014; Sinclair et al., 2005; Whitchurch et al., 2011). These thermochronological data show that significant denudation, around 8 km, occurred in the AZ with a peak between ca. 35 and 30 Ma along the central AZ, implying that the crust had been strongly shortened during Alpine convergence.

The earliest phase of cooling related to orogenesis has been constrained to be around 75–70 Ma (Figure 2), essentially based on detrital apatite and zircon thermochronological analyses of the central Pyrenean syn-orogenic sediments (Beamud et al., 2011; Mouthereau et al., 2014; Vacherat et al., 2017; Whitchurch et al., 2011), and in-situ analyses of Paleozoic bedrock of the Agly massif of the northeastern Pyrenees (Ternois et al., 2019). The onset of exhumation is less well constrained in the AZ, although few data suggest that Alpine cooling initiated around 65 Ma (Metcalf et al., 2009; Sinclair et al., 2005). Such early Cenozoic cooling would question the so-called quiescence phase described in the Pyrenees during Paleocene times (e.g., Grool et al., 2018; Rosenbaum et al., 2002 and references therein). The available thermochronological dataset from the AZ mainly constrain an onset of cooling at ca. 50-45 Ma (Figures 3 and 2; Fitzgerald et al., 1999; Garwin, 1985; Gibson et al., 2007; Jolivet et al., 2007; Maurel, 2003; Maurel et al., 2008; Metcalf et al., 2009; Sinclair, 2005; Yelland, 1991), long after the initiation of Alpine shortening at ~83 Ma. Based on these datasets the evolution of shortening in the Pyrenees has been considered to have occurred in two stages. During the initial Late Cretaceous stage of tectonic inversion, the orogenic wedge evolved symmetrically. Then, after closure of the distal domain of the rift, the Pyrenees developed asymmetrically from the Paleogene onwards (Grool et al., 2018; Jourdon et al., 2019; Mouthereau et al., 2014). The thermochronological data set mentioned above is mostly based on apatite thermochronology that best resolves the post-50 Ma cooling history, therefore there is the need for additional time-temperature constraints using thermochronometers with higher closure temperatures. Here, in addition to apatite fission-track and (U-Th)/He (AFT and AHe, respectively) ages, we provide new zircon fission-track and (U-Th)/He (ZFT and ZHe) analyses to better constrain the earliest cooling stages in the AZ and examine the distribution of denudation/shortening

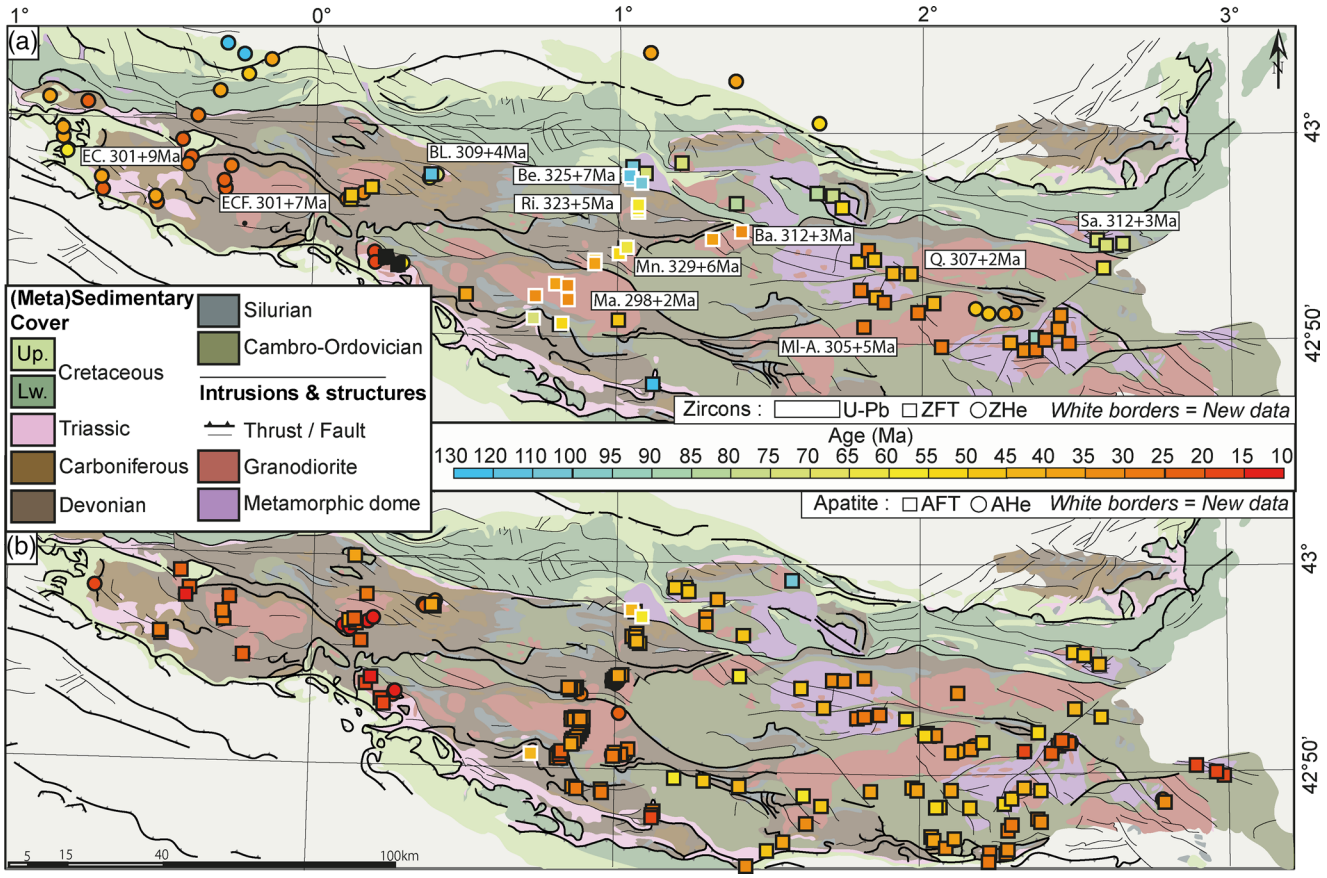

Figure 2. Low temperature thermochronological data in the Pyrenean Axial Zone (this study and Fitzgerald et al., 1999; Garwin, 1985; Gibson et al., 2007; Jolivet et al., 2007; Maurel, 2003; Maurel et al., 2008; Metcalf et al., 2009; Sinclair et al., 2005; Yelland, 1991) including new thermochronological data set (white borders): (a) zircon U-Pb (rectangle), zircon fission-track (square), zircon (U-Th)/He data (circle); (b) apatite fission-track (square), apatite (U-Th)/He (circle).

and its evolution through time. This new set of low-temperature (LT) thermochronological data is presented along a transect of the Central Pyrenees, few kilometers west of the ECORS-Pyrenees profile (Choukroune & the ECORS-Pyrenees Team, 1989, Figure 1). Time-temperature modeling of these data, integrated with literature data, provide a thermal history for each unit of the AZ. This allows to discuss (i) cooling of the AZ during Cretaceous rifting, (ii) the structural sequence and thermal evolution of the Pyrenees, (iii) the mode of shortening (distributed vs. localized, in-sequence vs. out-of-sequence), and (iv) the amount of Alpine versus Variscan shortening.

We show that the rift shoulder of the Iberian margin, that is, the future AZ, experienced significant denudation during mid-Cretaceous rifting. We also suggest that this southern margin was significantly heated during rifting: the geothermal gradient was probably as high as 40°C–50°C/km until Eocene times. Such a relatively high geothermal gradient most likely influenced the mode of shortening, as well as early softening of the crust (Airaghi et al., 2020; Bellahsen et al., 2019), distributed shortening during the early stages of convergence (until 50–40 Ma) as supported by our new thermochronological dataset.

2. Geological Setting

2.1. Variscan Orogeny and Mesozoic Rifting

The Variscan orogeny strongly affected the Paleozoic (meta)sediments of the Pyrenees during three distinct tectonic phases. D_1 deformation is associated with N-S compression (Denèle et al., 2009; Evans et al., 1997), which formed regional, kilometer-scale folds in the upper crust, while the lower crust experienced high-temperature and low-pressure (HT-LP) metamorphism (Cochelin et al., 2018). This stage of deforma-

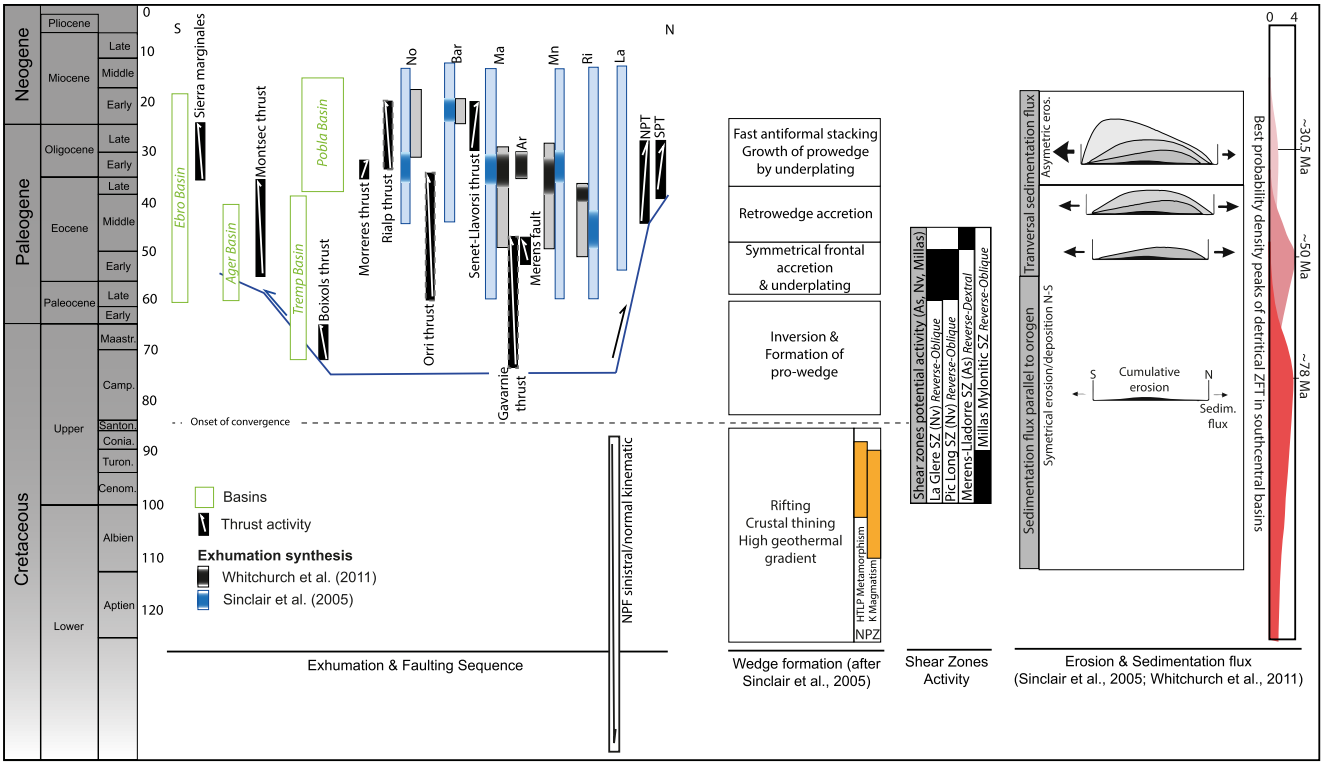

Figure 3. Synthesis of Mesozoic and Cenozoic events in the Axial Zone of Pyrenees (from Beamud et al., 2011; Bond & McClay, 1995; Deramond et al., 1993; Erdös et al., 2014; Filleaudeau et al., 2011; Fitzgerald et al., 1999; Labaume et al., 1985; Meigs & Burbank, 1997; Meigs et al., 1996; Metcalf et al., 2009; Mouthereau et al., 2014; Puigdefàbregas & Souquet, 1986; Rahl et al., 2011; Sinclair et al., 2005; Whitechurch et al., 2011). Nv: Neouvielle; As: Aston; Az: Arize; La: Lacourt; Ri: Riberot; Mn: Marimanya; Ar: Arties; Ma: Maladeta; Bar: Barruera; No: Nogueres; NPF: North Pyrenean Fault. NPT: North Pyrenean Frontal thrust; SPT: sub-Pyrenean thrust.

tion, estimated at around 325–320 Ma, probably induced moderate crustal thickening contemporaneous to metamorphism (Denèle et al., 2009; Laumonier, 2010). The D_2 deformation is represented by dextral transpressional flow dated at ca. 310 Ma in the migmatitic basement (Cochelin et al., 2018; Laumonier, 2010), transposed the initial schistosity S_1 into a subvertical $S_{1/2}$ schistosity (Druguet et al., 2009). This $S_{1/2}$ schistosity is the main fabric in the AZ. At the same time, the northernmost massifs in the upper crust underwent coaxial shearing, while the southern massifs mostly experienced non-coaxial shearing with top-to-the south shear zones (Cochelin et al., 2018). In the middle crust, compression formed mega-folds represented by successions of anticline and syncline of decakilometric wavelength (e.g., Couflens, Llavorsi; Figures 1 and 4a). Finally, at around 300 Ma, transpressive dextral deformation took place during emplacement of granitic to granodioritic plutons into the upper crust (Laumonier, 2010; Laumonier et al., 2014). This late Variscan deformation was associated with retrogressive Barrovian metamorphism.

After the collapse of the Variscan orogen during Permian times (e.g., Saspiturry et al., 2019; Vissers, 1992), a volcanic episode is commonly associated with Mesozoic extension. During the Jurassic, rifting in the Alpine Tethys domain was followed by the opening of the Ligurian and the central Atlantic oceans (Schettino & Turco, 2011), and later by the counter-clockwize rotation of Iberia (Montigny et al., 1986; Thinon et al., 2001). Around Albo-Cenomanian times, Pyrenean rifting induced crustal thinning (Golberg & Leyreloup, 1990), which resulted in a hyper-extended domain (Jammes et al., 2009; Lagabrielle & Bodinier, 2008; Lagabrielle et al., 2010; Masini et al., 2014, Saspiturry et al., 2019), accompanied by a high thermal gradient in the NPZ (Clerc & Lagabrielle, 2014; Vacherat et al., 2014). This stage is characterized by K-volcanism between 110 and 85 Ma (Figure 3; Montigny et al., 1986) and high-temperature (HT) metamorphism at ca. 95-93 Ma in the central Pyrenees (Albarède & Michard-Vitrac, 1978; Montigny et al., 1986). Maximal temperatures, constrained between 340 and 390 and 600°C (Golberg & Leyreloup, 1990; Vauchez et al., 2013), decrease from east to west as attested by RSCM (Raman Spectrometry on Carbonaceous Material) data (Clerc & Laga-

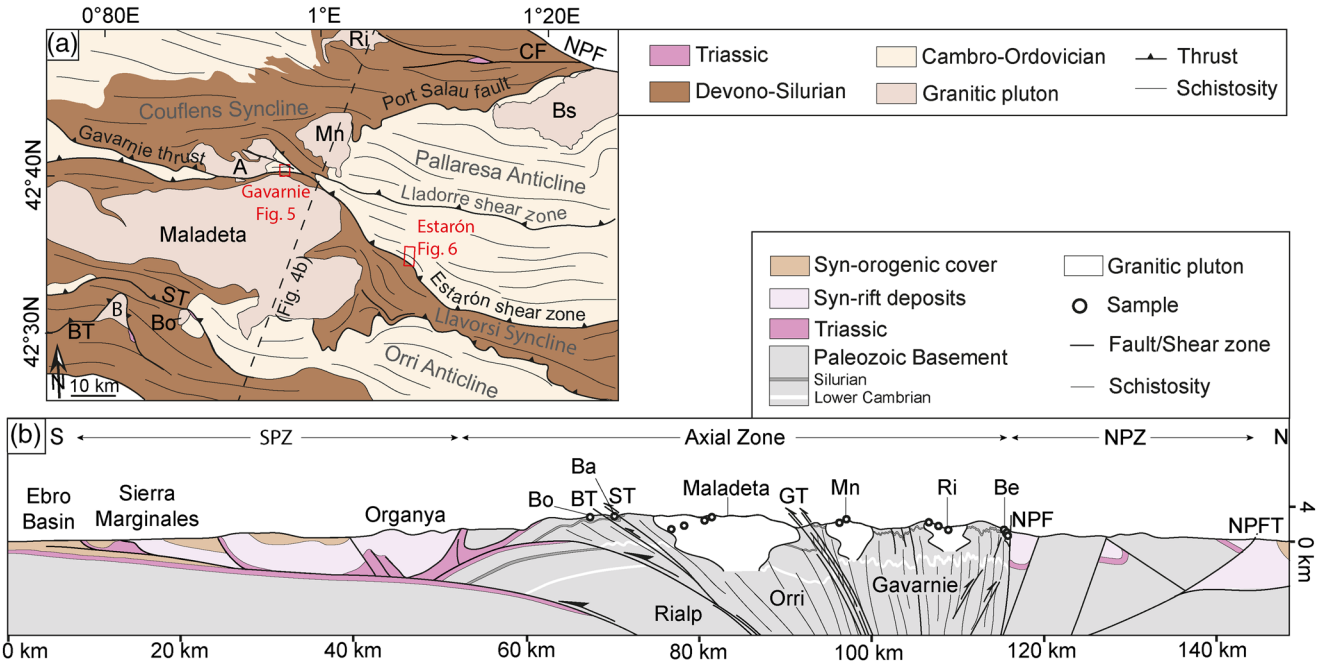

Figure 4. Structure of the Pyrenean wedge: (a) Structural map after Cochelin et al. (2018). (b) Cross-section of the Pyrenean wedge (few km west from the ECORS-Pyrenees profile). CF: Couflens fault system. A: Arties; B: Barruera; Bo: Bono; Bs: Bassies; Mn: Marimanya; Ri: Riberot; BT: Bono thrust; GT: Gavarnie thrust; NPF: North Pyrenean Fault; NPFT: North Pyrenean Frontal thrust; ST: Senet thrust.

brielle, 2014; Ducoux et al., 2018). These high temperatures are explained by crustal hyper-thinning and mantle exhumation witnessed by the occurrence of peridotites temporally and geographically associated with the mid-Cretaceous metamorphic and magmatic event (Clerc & Lagabrielle, 2014; Clerc et al., 2012; Jammes et al., 2009; Lagabrielle & Bodinier, 2008; Lagabrielle et al., 2010; Vielzeuf & Kornprobst, 1984). HT metamorphism is also recorded in extensional top-to-the-north mylonitic shear bands in the Saint Barthelemy gneiss (Figure 1; de Saint-Blanquat et al., 1990; Golberg & Leyreloup, 1990; Passchier, 1984; Vauchez et al., 2013) dated at 110-100 Ma (Costa & Maluski, 1988). In this massif, Mesozoic extension is also marked by a tectonic-hydrothermal event recorded by granite albitization at 117 Ma (Boulvais et al., 2007) and talc-chlorite mineralization dated at 112–97 Ma (Schärer et al., 1999).

2.2. Overview of the Alpine Shortening Sequence

Inversion of the mid-Cretaceous rift began in the late Santonian (Choukroune & the ECORS-Pyrenees Team, 1989; Muñoz, 1992; Mouthereau et al., 2014; Roure et al., 1989), coeval with the onset of the Iberia-Eurasia plate convergence, which is dated by the end of the Cretaceous Superchron at ca. 83 Ma. In the NPZ, the onset of orogenic cooling is recorded by 75–70 Ma old detrital AFT ages (Mouthereau et al., 2014) and by ~75 Ma in situ ZHe data (Ternois et al., 2019). The lack of cooling ages older than 75-70 Ma has been considered to be diagnostic of the transitional period from 83 to 75 Ma during which initial convergence occurred in abnormally hot Mesozoic basins located on the hyper-extended crust of the European margin (Mouthereau et al., 2014).

At 75-70 Ma, deformation shifted to the south where a thicker continental margin was shortened, as shown by the inversion of the Organya basin in the SPZ (Figure 1). There, the Bóixols thrust (Figure 1) is dated by illite $^{39}Ar/^{40}Ar$ dating at ca. 72 Ma (Rahl et al., 2011) and by a Campanian-Maastrichtian unconformity sealed by upper Paleocene cover rocks (Bond & McClay, 1995; Deramond et al., 1993). Orogenic cooling began in the NPZ at around 75-70 Ma (Figure 3) according to FT ages (Yelland, 1991) and inverse modeling of AFT data from foreland sediments (Mouthereau et al., 2014), including granitic cobbles and pebbles (Beamud et al., 2011). The early stage of Alpine cooling of the eastern Pyrenees is also recorded by detrital ZFT and ZHe data from southern basins (Beamud et al., 2011; Filleaudeau et al., 2011; Ternois et al., 2019;

Whitchurch et al., 2011, Figure 3). However, along the ECORS profile, orogenic cooling in the AZ is not well resolved by low-temperature (LT) thermochronology in the period spanning around 75 to ca. 50 Ma (Fitzgerald et al., 1999; Sinclair et al., 2005). MDD thermal modeling of K-Feldspar $^{39}Ar/^{40}Ar$ data tends to show reheating around 65 Ma which were interpreted with an early Cenozoic phase of shortening (Metcalf et al., 2009), associated with the slight (estimated to ca. 6–8 km) burial of the Maladeta massif to a maximum temperature of ~300°C under the Gavarnie unit. During late Cretaceous, the Gavarnie thrust (or shear zone; Figure 1) is thus thought to be kinematically linked to southward displacement of the Bóixols thrust which took place around 72–65 Ma (Bond & McClay, 1995; Deramond et al., 1993; Rahl et al., 2011). To the west, according to late Eocene illite/muscovite $^{39}Ar/^{40}Ar$ cooling ages, the Gavarnie thrust seems to be much younger (Rahl et al., 2011; Abd Elmola et al., 2018).

The Montsec thrust (Figures 1 and 3) was active from 55 Ma (faulted Ypresian growth strata, Cande & Kent, 1992) to 36 Ma (sealed by Roda sandstones, Meigs & Burbank, 1997; Meigs et al., 1996). Displacement on the Montsec thrust is classically interpreted to be linked to the Orri thrust activity (e.g., Mouthereau et al., 2014; Muñoz, 1992; Roure et al., 1989), which permitted the onset of cooling of the Maladeta (Orri unit) at around 50 Ma (Metcalf et al., 2009). Furthermore, part of the shortening associated with this period may also have been accommodated by internal deformation in the Gavarnie unit (Mouthereau et al., 2014). This period of regional exhumation in the AZ is also marked by the activation of the Merens sinistral-reverse fault (and potentially the Lladorre shear zone, Cochelin et al., 2018), at around 50 Ma (McCaig and Miller, 1986), and shear zones in the Neouvielle massif further west (48 Ma, Wayne and McCaig, 1998).

Published LT-thermochronological data suggest an increase of exhumation rate up to 173 ± 80 m/Myr in the northern AZ at ca. 50 Ma (Garwin, 1985; Fitzgerald et al., 1999; Sinclair et al., 2005). In the AZ, AFT cooling ages support Eocene exhumation in the Gavarnie and Orri massifs (Fitzgerald et al., 1999; Gibson et al., 2007; Sinclair, 2005). These data are interpreted to reflect the migration of deformation from N to S (Fitzgerald et al., 1999; Sinclair et al., 2005; Whitchurch et al., 2011). Detrital AFT ages of Beamud et al. (2011) in south-central basins support an exhumation rate of around 200 m/Myr in the AZ. These relatively high exhumation rates are consistent with the relatively high Pyrenean paleo-topography estimates by Huyghe et al. (2012) of up to ca. 2,000 ± 500 m around 49-41 Ma.

In late Eocene – Oligocene times, between 36 Ma and 25 Ma shortening localized along the Sierra Marginales thrust (SMT) (Figures 1 and 3). The SMT is sealed by 24.7 Ma lacustrine deposits (Meigs & Burbank, 1997; Meigs et al., 1996). From 36 to 27 Ma, the Morreres back-thrust (MBT) was also active (Figure 3). These two structures accommodated a total shortening of ca. 20 km, rooted in the Rialp basement thrust (Figures 1 and 3; Meigs et al., 1996; Mouthereau et al., 2014). According to AFT data from Maladeta, exhumation rates attained 2–3 km/Myr from 35 to 30 Ma (Fitzgerald et al., 1999; Gibson et al., 2007; Naylor & Sinclair, 2008; Sinclair et al., 2005). Modeling of track length from AFT data (Fitzgerald et al., 1999) and AHe ages (Metcalf et al., 2009) highlight a significant drop of cooling rate after ca. 32 Ma. Post-orogenic times are considered to start at around 25-20 Ma (Mouthereau et al., 2014).

2.3. Studied Plutonic Massifs

The plutons of the AZ were emplaced during late Variscan times (Bouchez & Gleizes, 1995; Evans et al., 1997; Gleizes et al., 1998) from ca. 340 to 290 Ma (Figure 2) at shallow upper crustal levels, as indicated by contact metamorphism of Carboniferous sediments. The granite and granodiorite composing the massifs eventually recorded some late/post Variscan dextral-reverse deformation under sub-solidus conditions (Cochelin et al., 2018).

The Bethmale granitic massif is the northernmost pluton of our study area, and contrary to the Maladeta massif in the core of the AZ, the Bethmale massif is exposed and sampled only at lower elevations, from ca. ~500–1500 m (Figures 1 and 3). The NPF separates the Bethmale granite from the NPZ (Figure 1). The Bassies and Bordères-Louron massifs were also sampled and respectively dated at 312 ± 3 Ma and 309 ± 4 Ma by U-Pb on zircon (Gleizes et al., 2006). These two massifs were emplaced during the Variscan transpressive D_2 phase (Druguet et al., 2009).

The Riberot, Marimanya and Arties massifs are located in the Gavarnie unit (Figure 1). The Riberot pluton crops out at high elevation between ~1,000 and ~2,300 m. The Carboniferous and Triassic rocks found a few kilometers to the east along the Couflens fault (Figures 1 and 2) provide a constraint for the top basement position in this area. Further south, the Arties and Marimanya plutons are located few km away from each other and are not separated by any major Alpine structure. Thus, they will be considered as part of the same tectonic unit and their samples used in the same age-elevation diagram (see below, 1,400–2,000 m for the Arties massif and 2,200–2,700 m for Marimanya massif; Figure 4). These massifs are located just north of the so-called Gavarnie thrust (Figure 1).

Within the Llavorsi syncline, in the northern part of the Orri unit, the Maladeta pluton was emplaced at ca. 298 ± 2 Ma (Evans, 1993, Figure 2). This massif shows a large range of elevations (from ~1,000 to ~3,000 m). According to Metcalf (2009), its Mesozoic shallow depth is supported by MDD thermal modeling of biotite and K-feldspar $^{39}Ar/^{40}Ar$ data, which suggest fast cooling below 350°C after emplacement. In the southern part of Orri, two small sampled plutons are separated by the Bono thrust: the Barruera and Bono plutons, which were emplaced into Devonian sedimentary rocks (Figures 1, 2, and 4a).

3. Structural Analysis of the Central Axial Zone

About 10 km west of the ECORS profile, we constructed a ~220 km-long cross-section from the Aquitanian to the Ebro basins (Figure 4b), including most of the studied massifs. Paleozoic (meta)sediments are subdivided into two stratigraphic units including Precambrian-Cambrian-Ordovician and Devonian-Carboniferous units. These two units are separated by Silurian black slates, commonly considered as a décollement surface (e.g., Clariana & García-Sansegundo, 2009; Cochelin et al., 2018; García-Sansegundo et al., 1997). As a marker of the Meso-Cenozoic Alpine deformation, the Triassic layers are specifically outlined in the cross section. The external parts (such as the NPZ and SPZ) are mainly based on the restoration of Mouthereau et al. (2014).

The sub-vertical NPF separates the NPZ from the AZ. This structure is classically considered as an inherited extensional low-angle detachment (Clerc & Lagabrielle, 2014; Lagabrielle et al., 2010), its vertical attitude being explained by the tilting of the Gavarnie unit. As such tilting has been questioned recently (Cochelin et al., 2018), we propose an alternative structural evolution in the discussion. In the northern AZ, the main schistosity (i.e. foliation in basement rocks characterized by the presence of phyllosilicates) is steeply dipping and associated with coeval north verging folds, small-scale shear zones and north-verging kink bands.

The Couflens syncline located in the northern Gavarnie unit is bordered by the NPF and the by Port Salau fault (east of Marimanya) or Gavarnie thrust (westward; Figure 4a). In the syncline, some remaining Triassic deposits crop out close to the Couflens fault zone (Figures 1 and 4a; Ternet et al., 2004). South of the Couflens syncline, the Pallaresa anticline which affected the Cambro-Ordovician series, was deformed by the Lladorre shear zone (western continuation of the Merens shear zone), which was activated at around 50 Ma (Denèle et al., 2008; A. McCaig, 1986; Mezger et al., 2012). In the western part of the Pallaresa anticline, many shear zones attest for distributed shortening in the Paleozoic rocks in the lateral continuation of the Gavarnie thrust (Figure 5). Between the Maladeta and Marimanya massifs, the Paleozoic layers are affected by a main penetrative 60–80°N-dipping schistosity that are cross cut by top-to-the-south shear zones (Figure 5). This deformation can be observed along at least 100 m north of the Gavarnie "thrust" (Figure 4a), which is usually considered as the major Alpine structure in the AZ, accommodating 10–20 km of displacement (A. McCaig, 1986; Mouthereau et al., 2014; Muñoz et al., 1992; Seguret, 1972). However, several authors argued that such displacement only occurred in the western AZ (Cochelin et al., 2018; Soler et al., 1998).

The Estarón shear zone, considered as an eastern prolongation of the Gavarnie thrust, is less clearly defined (Figure 6). Several smaller-scale shear zones can be observed and a large, overhanging north-dipping fold limb separates the Pallaresa anticline and the Llavorsi syncline (Figure 4). In this area, the main schistosity and top-to-the-south shear zones have a shallower dip (<45°N, Figure 6a) than north of the Gavarnie unit. The schistosity and shear zones affected mica-rich rocks mainly composed of quartz, white mica and biotite.

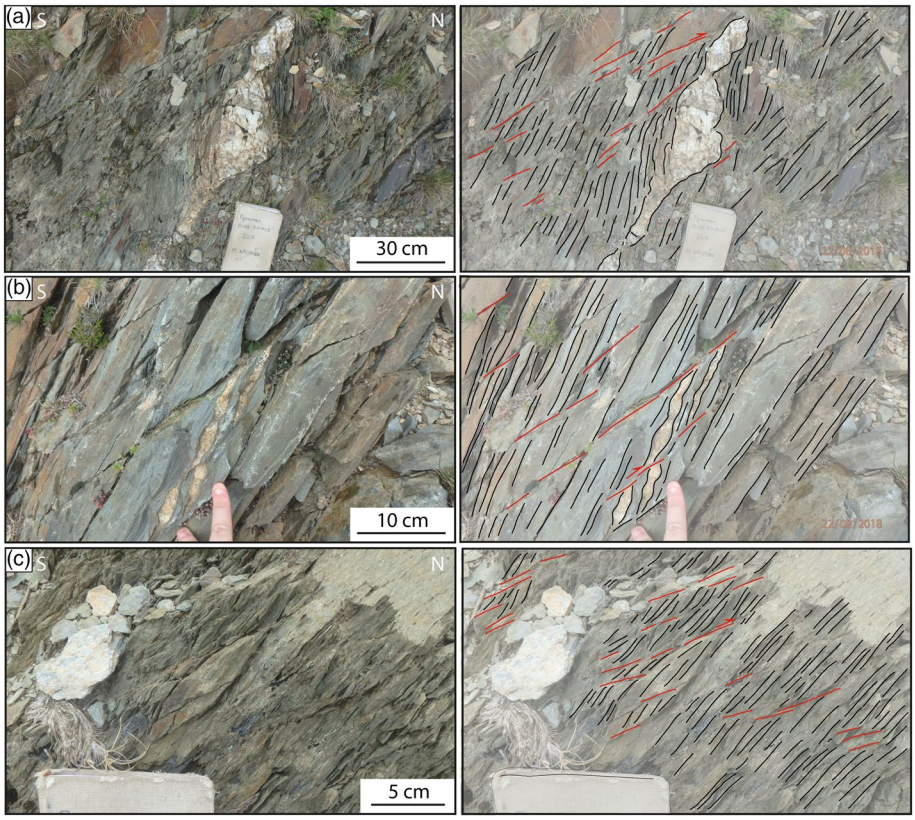

Figure 5. Mesoscale structures in the Gavarnie shear zone between Marimanya and Maladeta: (a), (b), and (c) are located at a distance of about 100 m from each other and define a zone of distributed deformation of several hundreds of meters.

In Devonian rocks, south of the Maladeta massif (Figure 4), the main schistosity dips at shallow angles (from 25 to 50°N). Between the Bono and Maladeta plutonic massifs, the south-verging Senet-Llavorsi and Bono thrusts deformed Triassic rocks, attesting for their Alpine age. The southern Orri unit (near Bono and Barruera) is mostly composed of Devonian to Silurian sedimentary rocks and south-verging shear zones associated with a slightly less penetrative main schistosity compared to the Gavarnie unit.

Thus, in the AZ, there are several evidences of distributed deformation within Paleozoic schists, such as penetrative schistosity, observed at least up to 200 m away from the main shear zones/thrusts. In the absence of Mesozoic rocks and geochronological dating, these deformations can be attributed either to Variscan or Alpine cycles, or both. We propose that part of this schistosity was formed during the Alpine orogeny as strongly suggested by thermochronological data shown below.

4. Methodology

4.1. Sampling Strategy

Nineteen granitic to granodioritic samples were collected in nine plutonic massifs along vertical profiles, following the ECORS-Pyrenees profile in the AZ (Figures 2a and 2b). Samples were prepared for several LT-thermochronological analyses (AFT and ZFT). In the northernmost part of the AZ, three samples were collected in the Bethmale massif, one in the Bordères-Louron massif. Further south, two samples were collected in both the Marimanya and the Arties massifs and three samples in the Riberot massif. Those massifs are in the Gavarnie unit (*s.l.* in the core of the AZ), four samples were also collected in the Maladeta pluton, in the Orri unit. Rocks were sampled only in the central part of the massif (Figure 1), which is aligned with the other smaller massifs further north (Bethmale, Riberot, Marimanya, Arties). Finally, in the south, one sample was collected both in the Barruera and in the Bono plutons.

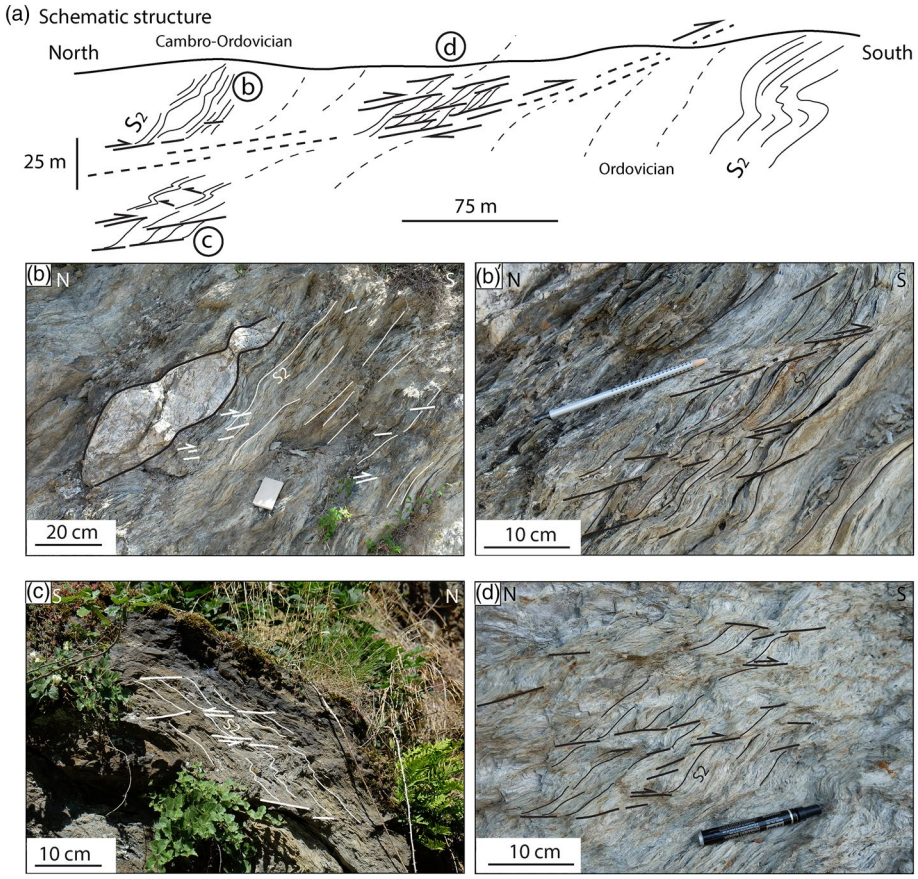

Figure 6. Mesoscale structures in the Estarón shear zone. (a) N-S Schematic cross-section, not exactly at scale. Shear intensity increases from (b) and (c) to (d).

Zircon and apatite grains were separated for LT-thermochronological analyses using standard heavy-liquid and magnetic separation techniques in the Center de Recherches Pétrographiques et Géochimiques (CRPG) (Nancy, France). Minerals were finally hand-picked to keep a large fraction of apatite and zircon between 75 and 400 μm.

4.2. Zircon and Apatite Fission-Track

Apatite and zircon grains were analyzed at the ISTerre thermochronology laboratory (Grenoble Alpes University, France). Apatite grains were mounted in epoxy, polished to expose internal crystal surfaces, and etched with 5.5 M HNO_3 for 20 s at 21°C. Zircon grains were mounted in Teflon sheets, polished, and etched with NaOH-KOH at 228°C between 8 and 36 h. Using the external detector method (Gleadow et al., 1976), mica sheets were attached to all samples and irradiated at the FRM II Research Reactor of the Technische Universität München (Germany) together with IRMM 540R and IRMM 541 dosimeter glasses for apatite and zircon respectively. Fish Canyon Tuff age standards were also irradiated with apatite and zircon. After irradiation, mica detectors were etched in 48% HF at 21°C for 18 min. Counting was carried out at 1250x on Olympus BH2 and BX51 optical microscopes using FTStage 4.04 system (Dumitru, 1993). Individual fission-track ages were obtained using zeta factors following the approach of Hurford and Green (1983). Horizontal confined track lengths and track etch pit size were measured to determine the Dpar value for apatite samples. The fission-track data are presented below in radial plots made with the RadialPlotter software of Vermeesch (2009) which also permitted to discriminate several age populations (see the supporting information Table S4 for formatted fission-track data).

Note Table 1. Ages were calculated using the zeta: 279.98 ± 13.35 for AFT data, 124.08 ± 2.95 for zircon fission-track data from Arties, Maladeta, Barruera, Bono and Bordères-Louron massifs, and 131.44 ± 4.05 for Bethmale, Riberot, Marimanya and Bassies massifs. Rho-S: Spontaneous track density (track/cm^2), number of measured tracks in brackets; Rho-I: Induced track density (track/cm^2), number of measured tracks in brackets; Rho-D: Effective track density (track/cm^2), number of measured tracks in brackets; Disp.: Dispersion of data (%); Dpar: Mean of the diameter of projected tracks (μm); Central ages are determined by Radialplotter software of Vermeesch (2009) with an error of two sigma; No. Xls: number of analyzed grains; P (X^2): Chi-square probability (%).

4.3. Zircon (U-Th)/He

Between two and four single zircon grains per sample were selected with prismatic to round shape, zero to two pyramids, and an equivalent spherical radius ranging from 50 to 110 μm. Conventional zircon (U-Th)/He (ZHe) analysis were performed in the noble gas laboratory and Service d'Analyze des Roches et des Minéraux (SARM) at CRPG (Lorraine University, France). Zircon were loaded in platinum capsules for He extraction, and were outgassed at 1500°C for 20 min using a diode U-V laser. Extracted gas has been subsequently purified in an all metal line and analyzed for He concentrations with a quadrupole mass spectrometer by addition of a ^{3}He spike. After total helium extraction, content of U, Th, and Sm was measured at the SARM following the procedure described in Tibari et al. (2016). Zircon ages were corrected for α ejection (FT) following Ketcham et al. (2011). The global precision of He ages determined with this procedure is within 6%–8 % (1σ), and yield a Fish Canyon Tuff (FCT) age of 28.6 ± 2.5 Ma during the course of these measurements.

Note Table 2. ZHe ages are corrected for alpha ejection (FT parameter; Ketcham et al., 2011).

4.4. Modeling Approach

The thermal inversion involved the new thermochronological data set (Tables 1 and 2) and published records (Fitzgerald et al., 1999; Gibson et al., 2007; Metcalf et al., 2009; Sinclair et al., 2005). Those data were selected to keep a wide spread of elevations for each plutonic massif (see Table S4 for the complete modeled data). This multi low-temperature thermochronology dataset helps to determine the best time-temperature paths using a Bayesian "Markov chain Monte Carlo" algorithm implemented in the software QTQt (Gallagher, 2012; Gallagher et al., 2009). Several annealing models are implemented for AFT and ZFT (Ketcham et al., 2007; Tagami et al., 1998; Yamada et al., 2007). However, the available ZFT annealing models are calibrated for zircon with Miocene or younger apparent cooling ages or low uranium content, and with relatively low amounts of radiation damage. Low or undamaged zircon have fission-track closure temperatures in the range ca. 300°C–340°C (Rahn et al., 2004). However, older grains observed in Pyrenean plutons are commonly more damaged and associated with lower closure temperatures of around 240°C ± 20°C, of course depending on cooling rate (Bernet, 2009; Bernet & Garver, 2005; Brandon et al., 1998; Garver & Kamp, 2002). Hence, ZFT data from grains with significant amounts of radiation damage (commonly grains with older apparent cooling ages) could not be correctly inverted in QTQt modeling. Zircon from the plutons in the AZ are probably too much damaged to be considered correctly by available thermochronological models. Thus, ZFT records will be used as constrain boxes at around 240°C ± 50°C (Bethmale, Riberot, Marimanya, and Barruera massifs) and 280°C ± 50°C (Maladeta massif) for inverse thermal models. This difference can be explained by the fact the Maladeta massif has been slightly hotter than the others during Cenozoic times (Figure 2a), implying that its zircon are less damaged and probably associated with higher closure temperatures.

Recent models of He diffusion kinetics in zircon (Guenthner et al., 2013) and apatite (Flowers et al., 2009; Gautheron et al., 2009) are available in QTQt. Gautheron et al. (2009) explained AHe ages and He diffusion with a linear physical trapping He retention law calibrated for samples with old apparent AHe cooling ages of FeU-rich apatites. Apatites from the plutonic massif of the AZ show relatively young AHe ages. Therefore, the model from Flowers et al. (2009), which better constrains low damaged minerals, is used in our modeling approach. In this study, all grains from our ZHe dataset (Table 2) were inversed with published AHe data (see Table S4 for the complete thermochronological dataset in the central AZ).

Table 1
Fission Track Results From the Axial Zone, Pyrenees

Sample	Latitude	Longitude	Elevation *M*	Rho-S *(*10⁶)*	Rho-I *(*10⁶)*	Rho-D *(*10⁶)*	Dpar μ*m*	U *ppm*	No. *xls*	Disp. %	P (X^2) %	Central age *Ma*	±
Zircon													
Bethmale													
ZA16-55	42°53′27.22″N	**1°2′15.01″E**	720	10.9 (3994)	2.82 (1033)	4.68 (4272)		309	21	16	0	118.7	11.8
ZA16-54	42°52′35.10″N	1°2′55.59″E	1216	11.5 (3224)	3.05 (852)	4.677 (4269)		336	27	15	4	116.4	10.2
ZA16-62	42°51′34.42″N	1°6′20.00″E	1409	10.6 (3394)	2.96 (945)	4.683 (4275)		332	21	19	0	104.8	12
Borderes-Louron													
ZA18-03	42°53′19.39″N	0°23′3.57″E	1020	7.26 (1048)	1.86 (268)	4.87 (4040)		270	13	0	58	95.9	6.6
Riberot													
ZA16-14	42°48′1.43″N	1°3′32.97″E	1855	5.96 (4824)	2.81 (2270)	4.66 (4254)		291	30	19	0	59.4	7.6
ZA16-15	42°47′52.13″N	1°4′24.74″E	2279	6.64 (2889)	2.27 (989)	4.663 (4257)		249	28	46	0	93	17.6
ZA16-16	42°48′47.44″N	1°3′11.80″E	1452	6.41 (3006)	3.31 (1554)	4.667 (4260)		377	32	12	2	57.1	4.2
Marimanya													
ZA16-30	42°41′36.82″N	0°58′49.94″E	2250	6.92 (2526)	3.54 (1291)	4.67 (4263)		453	28	27	0	59.4	3.8
ZA16-50	42°42′31.94″N	1°0′43.88″E	2664	8.28 (1629)	3.33 (655)	4.673 (4266)		396	19	30	0	67.5	6
Arties													
ZA16-31	42°39′43.41″N	0°55′18.79″E	1690	4.93 (2096)	3.09 (1314)	4.162 (4298)		430	26	5.1	73	39.1	1.5
ZA16-32	42°40′51.46″N	0°55′42.89″E	2014	7.84 (3581)	3.06 (1397)	4.165 (4300)		392	32	13	2	65.1	2.6
Maladeta													
ZA16-20AB	42°35′26.93″N	0°51′27.48″E	1850	5.13 (3839)	3.71 (2777)	4.153 (4290)		485	17	5.2	26	33.6	1
ZA16-25AB	42°35′48.35″N	0°45′36.83″E	1463	4.24 (1963)	2.94 (1363)	4.155 (4292)		399	23	0	51	34.4	1.3
ZA16-27A	42°37′23.37″N	0°49′37.71″E	2551	5.06 (2205)	3.7 (1612)	4.157 (4294)		512	21	0	41	30.6	1.2
ZA16-28	42°38′20.99″N	0°48′25.39″E	2338	6.02 (3390)	3.89 (2191)	4.16 (4296)		522	25	5.1	23	35.5	1.1
Barruera													
ZA17-46	42°31′25.16″N	0°49′14.39″E	1355	8.75 (3524)	4.15 (1669)	4.167 (4302)		556	28	12	2	51.6	2
Bono													
ZA17-54	42°32′40.83″N	0°43′50.34″E	1100	11 (2776)	2.87 (721)	4.169 (4303)		388	25	19	0	91.5	5.5
Bassies													
ZA16-11	42°44′39.43″N	1°18′47.42″E	1912	7.5 (2149)	5.18 (1482)	4.65 (4248)		572	32	24	0	47	5
ZA16-13	42°45′15.92″N	1°22′55.26″E	1652	6.66 (2113)	4.08 (1294)	4.657 (4251)		477	32	46	0	50.2	9
Apatite													
Bethmale													
ZA16-54	42°52′35.10″N	1°2′55.59″E	1216	0.298 (275)	1.25 (1153)	1.335 (4020)	1.06 ± 0.22		21	0	79	46.4	3
ZA16-62	42°51′34.42″N	1°6′20.00″E	1409	0.362 (210)	1.22 (707)	1.336 (4019)	1.13 ± 0.25		20	0	83	55.5	4.4
Bono													
ZA17-54	42°32′40.83″N	0°43′50.34″E	1100	0.22 (271)	0.983 (1212)	1.338 (4018)	1.36 ± 0.31		21	0	68	43.6	2.8

During inversion, the QTQt software first defines a random time-temperature path and kinetic parameters allowing the modeling of the observed data. Then, initial conditions are slightly modified and synthetic data are compared to the input dataset. The best-fit model is compared to the observed data, conserved, and the operation is repeated until the model is considered as stable. Between 500,000 and 1,000,000 runs were performed on each model depending on their stability (likelihood and posterior chain; see Gallagher, 2012).

The final expected model shows a range of time-temperature paths associated with probability calculated in time-temperature space. This statistical information is used to evaluate confidence level.

Our inverse modeling of low-temperature data was performed on four massifs from different tectonic units. They have been selected to represent the cooling history of each part of the AZ: the northernmost massifs (Bethmale), the northern massifs (Riberot and Marimanya-Arties), the central massif (Maladeta), and the southern massifs (Barruera). As reported previously, zircon U-Pb crystallization ages from plutonic massifs cluster around 305 ± 5 Ma in the AZ and NPZ (Gleizes et al., 2006; Maurel et al., 2003; Olivier et al., 2008; Paquette et al., 1997; Respaut et al., 1983; Roberts et al., 2000; Ternet et al., 2004; Vacherat et al., 2014). These temperatures are set as initial boundary conditions with temperatures around 800°C ± 100°C reached during pluton emplacement (constraint box, see Figure S3) followed by fast cooling to 300°C ± 50°C at about 295 Ma (see Figure S3). A constraint box constrains the position of the plutons close to the surface during Permo-Triassic times (see Figure S3). The younger constraint box is placed according to available ZFT data.

5. Results

5.1. Zircon Fission Track Data (ZFT)

Nineteen samples containing between 18 and 32 grains from 9 massifs in the AZ were analyzed (Table 1). Each age or age population was interpreted considering dispersion, P (X^2), and variation of uranium content to determine central and peak ages and error (2σ). We considered that a sample most likely has several age populations when the following conditions are met: a dispersion above 10%–15% (see below for exceptions) and a null P (X^2) value. In such case, peak ages are considered instead of central ages. Central and peak ages were determined with the Radialplotter software (Vermeesch, 2009).

Near the NPF, the samples from the Bethmale massif show a dispersion of 12%–19%, whereas the Radialplotter software suggests only one age population, with a Late Cretaceous central age (Figures 7b and 7d) from 104.8 ± 6 in ZA16-62 (1,409 m) to 118.7 ± 11.8 Ma in ZA16-55 (720 m). The sample from the Bordères-Louron massif ZA18-03 also shows a Late Cretaceous central age at 95.9 ± 6.6 Ma (Figures 7c and 7e). The less elevated sample from the Bassies massif (Figures 7c and 7e) shows a strong dispersion (46%) and also a Late Cretaceous population around 117 ± 23 Ma, highlighted by the grains with the lowest uranium content.

The central massifs from the Gavarnie unit show younger ZFT ages than the northernmost ones. The samples from the Riberot massif show an increase of dispersion with elevation and a P (X^2) equal to zero except at low elevation (Figures 8b and 8d). The peak fitting algorithm yields three age populations for the most elevated sample ZA16-15 (2279 m). The grains with the lowest uranium content fall into the 326 ± 63 Ma (pop. ~14%) and 109 ± 9 Ma (pop. ~46%) peaks, whereas zircon with the highest content of uranium show a Paleocene age population of 60.9 ± 4 Ma. Sample ZA16-14, located at a lower elevation of 1855 m, shows ages with lower dispersion (19 %) and only two populations, namely a Late Cretaceous one (80 ± 6 Ma) and a Paleocene one (59 ± 2 Ma). Sample ZA16-16 from the base of the Riberot vertical profile (1452 m) has a lower dispersion (12%) and only one age population of 57.1 ± 2.1 Ma.

A similar trend is observed on the samples from the Marimanya massif. Sample ZA16-50, located at 2,664 m of elevation, yields two age populations at 111 ± 17 Ma and 62.8 ± 5.3 Ma (Figures 8c, and 8e). Despite a slight decrease of dispersion, the lower-elevated sample (2,250 m; Figure 8c) still shows two age populations at 89 ± 11 Ma and 51.8 ± 3.4 Ma. In the Arties pluton, the most elevated sample ZA16-32 (2,014 m; Figures 8c and 8e) shows two populations at 72.3 ± 3.6 Ma and 48.9 ± 4.2 Ma. The other sample ZA16-31 (1,690 m; Figure 8c) shows only one population at 39.1 ± 1.5 Ma with a low dispersion (5%) and a higher P (X^2) of 72%.

In samples from the Maladeta massif (Figures 9b and 9e), we obtained ages from 30.6 ± 1.2 Ma to 35.5 ± 1.1 Ma, from 1,463 to 2,551 m elevations, respectively (Table. 1), with a low dispersion (≤5%) and an average P (X^2) of ~ 0.35.

In the southern part of the AZ, a sample from the small Barruera pluton, located at low elevation (Sample ZA17-46, 1,355 m; Figure 9c) shows a central age of 51.6 ± 2 Ma with an age dispersion of around 12% and a P (X^2) at 2 %. Sample ZA17-54 from the Bono pluton has a central age of 91.5 ± 5.5 Ma (Figure 9d), but con-

Table 2
Zircon (U-Th)/He From the Axial Zone, Pyrénées

Sample	Latitude	Longitude	Elevation *M*	Length *μm*	Width *μm*	Radius *μm*	Mass *μg*	U *ppm*	Th *ppm*	Sm *ppm*	eU *ppm*	±	FT	4He *nmol/g*	Corrected age *Ma*	±
Bethmale																
ZA16-62-1	42°52′35.10″N	1°2′55.59″E	1409	138	97	49	3.2	682	209	15	731	51	0.77	137.9	45.4	2.7
ZA16-62-2				208	112	64	7.7	133	53	1	145	20	0.81	73.8	116.1	11.8
ZA16-62-3				131	53	33	1.2	1562	482	32	1672	129	0.64	306.5	53.0	2.7
ZA16-54-1	42°52′35.10″N	1°2′55.59″E	1216	220	89	55	5.9	200	57	1	213	25	0.78	103.3	115.5	10.1
ZA16-54-2				302	159	91	22.9	287	98	6	310	11	0.87	103.5	71.6	2.5
ZA16-54-3				115	81	41	1.9	1151	270	16	1214	84	0.73	259.5	54.3	2.8
ZA16-54-4				191	78	48	3.9	217	63	2	232	37	0.75	103.1	110.1	12.5
ZA16-54-5				241	121	71	10.9	457	113	3	483	20	0.83	193.3	89.6	3.4
Riberot																
ZA16-15-4	42°47′52.13″N	1°4′24.74″E	2278	245	96	60	7.8	239	92	13	260	21	0.79	47.5	42.6	3.0
ZA16-15-5				226	99	60	7.3	212	86	12	132	22	0.80	132.7	133.1	9.8
ZA16-16-1	42°48′47.44″N	1°3′11.80″E	1452	238	130	74	11.9	396	108	23	421	18	0.84	79.9	42.1	1.7
ZA16-16-3				216	125	69	9.6	807	121	7	835	30	0.83	193.9	52.0	2.1
ZA16-16-4				252	124	73	12..1	208	29	7	215	13	0.83	114	118.0	6.7
ZA16-16-5				176	86	51	4	1547	255	10	1607	61	0.76	293.6	44.4	1.7
Marimanya																
ZA16-30-1	42°41′36.82″N	0°58′49.94″E	2250	274	84	55	7.2	311	138	6	343	23	0.77	142.7	99.7	5.5
ZA16-30-2				286	118	73	13.4	207	93	5	229	13	0.83	75.6	74.0	3.5
ZA16-30-3				208	94	57	5.9	338	85	0	358	26	0.78	53.3	35.2	2.1
ZA16-30-4				260	84	55	6.7	404	63	2	419	24	0.77	69.3	39.7	1.9
ZA16-30-5				198	84	51	4.6	492	242	5	549	36	0.76	100.2	44.4	2.3
ZA16-50-4	42°42′31.94″N	1°0′43.88″E	2664	147	92	49	3.4	418	102	2	442	45	0.77	79.8	43.7	3.4
ZA16-50-5				167	70	43	2.7	1180	220	13	1232	64	0.72	219.6	45.8	2.0
Arties																
ZA16-31-1	42°39′43.41″N	0°55′18.79″E	1690	227	112	66	8.8	669	159	2	706	27	0.81	109.6	35.3	1.2
ZA16-31-3				229	62	41	3.3	681	266	9	743	50	0.70	143.9	51.0	2.4
ZA16-31-5				277	108	68	11.2	333	105	5	358	17	0.82	72	45.7	2.2
Barruera																
ZA17-46-1	42°31′25.16″N	0°49′14.39″E	1355	212	72	46	3.9	588	196	5	634	42	0.74	108.8	43.3	2.2
ZA17-46-2				178	80	48	3.7	376	143	3	410	42	0.75	82.9	50.1	3.6
ZA17-46-4				197	74	47	3.7	795	204	−1	843	46	0.74	113.1	33.6	1.4
ZA17-46-5				292	79	52	6.9	441	133	2	473	26	0.76	83	42.6	2.3
Bono																
ZA17-54-1	42°32′40.83″N	0°43′50.34″E	1100	165	63	40	2.3	1087	346	35	1168	73	0.70	83.9	19.1	0.8
ZA17-54-2				205	85	52	5	442	149	25	477	32	0.77	88.4	44.8	2.4
ZA17-54-3				227	100	61	7.4	768	195	9	813	31	0.80	64.8	18.5	0.7
ZA17-54-4				247	107	65	9.3	223	89	11	244	18	0.81	48.6	45.6	2.6

sidering the dispersion of ages at 19% and the null P (X^2) two populations at 112 ± 11 Ma and 74.8 ± 7.3 Ma can be distinguished (Figures 9d and 9f).

As shown above, most of the samples show a strong dispersion and several populations, especially in the northern Bethmale and Bassies massifs (Figure 7). The samples at the highest elevation from the north-central Riberot and Marimanya plutons also show several age populations (Figure 8). No such dispersion is observed in the samples from the core of the AZ represented by the Maladeta massif (Figures 9b and 9e).

5.2. Apatite Fission Track (AFT)

We focused the acquisition of AFT ages on the few massifs where no such data were available in the literature. Contrary to ZFT data, AFT data show high P (X^2) results (between 68% and 83%; Table 1; Figure S1). Samples from the Bethmale massif show AFT central ages of 55.5 ± 4.4 Ma at 1,409 m elevation and 46.4 ± 3 Ma at 1,216 m elevation (Table 1). In the southern AZ, the sample from the Bono massif has an age of 43.6 ± 2.8 Ma at 1,100 m elevation.

5.3. Zircon (U-Th)/He (ZHe)

Zircon (U-Th)/He dating was performed on 10 samples (each composed of 2–4 grains) from the same massifs as for FT dating (Table 2). The results (Figure 10) show a strong dispersion and age populations with three distinct populations: (i) from 118 ± 6.7 to 89.6 ± 3.4 Ma for the northernmost plutons (Bethmale and Riberot), (ii) from 54.3 ± 2.8 Ma to 35.3 ± 1.2 for all massifs, and (iii) at 19.1 ± 0.8 Ma and 18.5 ± 0.7 Ma for the southernmost Bono pluton (Figures 10a and 10b. Most of ZHe ages are between AFT and ZFT ages (Figure 10b).

No correlation is observed between the ZHe ages and the equivalent spherical radius (ranging from 50 to 90 μm). However, the variation of effective uranium content (eU = U + 0.235 Th) is a potential source of age variation for zircon (Guenthner et al., 2013). By plotting ZHe ages against eU content, two major populations of age can be constrained (Figure 10a). Indeed, low eU content (<250 ppm) yield ZHe age around 120 Ma, while high eU (>250 ppm) yield ages rather around 45 Ma.

5.4. Age-Elevation Relationships

Exhumation rates are estimated from age-elevation relationships of FT data (Figure 11). Considering that the youngest age population is the least retentive population of zircon, they are more easily reset during the main orogenic event. Thus, in case of samples affected by several age populations, for the construction of age-elevation relationships, we selected the youngest age population (P_1) determined by Radialplotter. However, we should note that the central age-elevation trend of the northern plutonic massifs (Riberot, Marimanya, and Arties) highlights a break in slope between 1,800 and 2,000 m of elevation (Figures 11b). In the Bethmale massif (Figures 11a and 11c), negative correlations for ZFT ages do not permit to estimate exhumation rates.

A few kilometers to the south, in the Riberot massif, AFT and ZFT age-elevation profiles point to a constant exhumation rate of ca. 200 ± 50 m/Myr from Paleocene to mid-Eocene times (Figure 11d). The uncertainty, for each rate (also in the following), is calculated by estimating the slowest and fastest exhumation compatible with our data and according to their own uncertainty. In the Marimanya and Arties massifs, estimated exhumation rates only attain 40 ± 10 m/Myr (Figure 11e, see Figure S2) from Paleocene to mid Eocene times, but they increase to ca. 200 ± 50 m/Myr from late Eocene to Oligocene times (at least until ca. 30 Ma).

To the south, ZFT data indicate higher exhumation rates > 800 m/Myr in the Maladeta pluton (Orri unit) from ca. 35 to 30 Ma. Subsequently, exhumation significantly decreased to 160 ± 90 m/Myr until at least 25 Ma (Figure 11f). By contrast to AFT data, the ZFT age-elevation trend from the same massif reveals that the rate of exhumation does not vary much with elevation. As a consequence, the exhumation rate of the Maladeta massif has been calculated neglecting the highest sample and could be considered as a minimal exhumation rate. In the Barruera massif, in the southern part of the Orri unit, the AFT age-elevation relationship gives an average exhumation rate at ca. 225 ± 50 m/Myr around 20 Ma (Figure 11g).

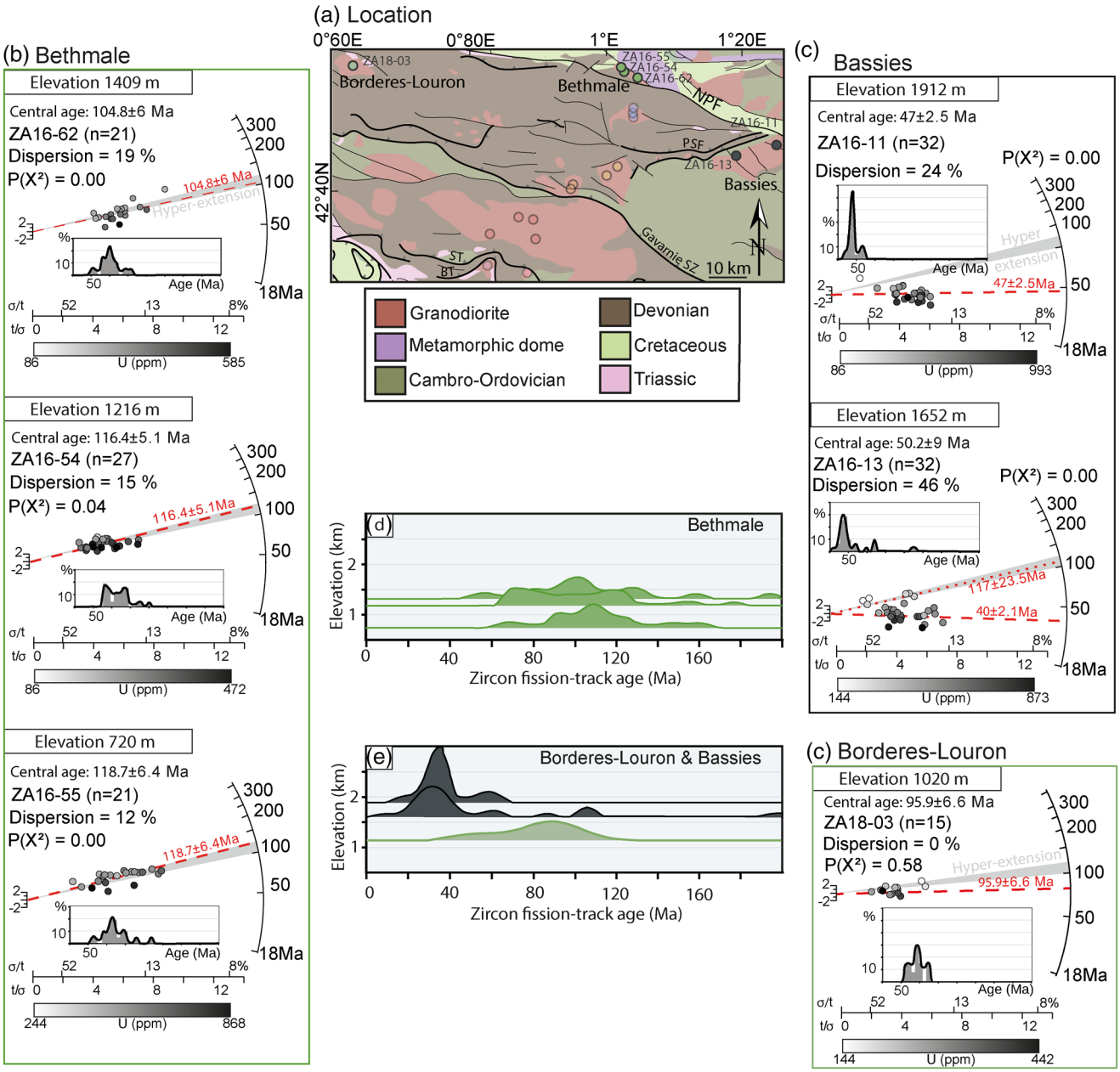

Figure 7. Detailed ZFT records for the northernmost massifs (Radialplot & density plot obtained by Radialplotter software): (a) location of ZFT samples, plutonic massifs and major structures (BT: Bono thrust; NPF: North Pyrenean Fault; PSF: Port Salau Fault; ST: Senet thrust). (b and c) Radialplots including the Cretaceous hyper-extensional phase (*light gray*). (d and e) Age density plot versus elevation for Bethmale, Bassies, and Bordères-Louron massif (in *dark green*, *black*, and *gray*, respectively).

5.5. Inverse Thermal Modeling

In these massifs, QTQt modeling only predict the youngest Paleocene-Eocene ZHe ages despite the Cretaceous population (Figures 12a–12e). This observation concerns three zircons used for (U-Th)/He from the Bethmale and the Riberot massifs (respectively in ZA16-62 and ZA16-15; Table 2; Figures 7a and 8a). Predicted AHe ages for samples from Barruera show slightly older ages than the expected ages, but suggest a similar cooling rate. There is a general good fit between predicted and observed AFT ages for all massifs, except for the Barruera massif, where predicted AFT ages are slightly older than observed ages. The expected time-temperature (t-T) path of the Bethmale pluton (Figure 12f) shows an isothermal or very slow cooling

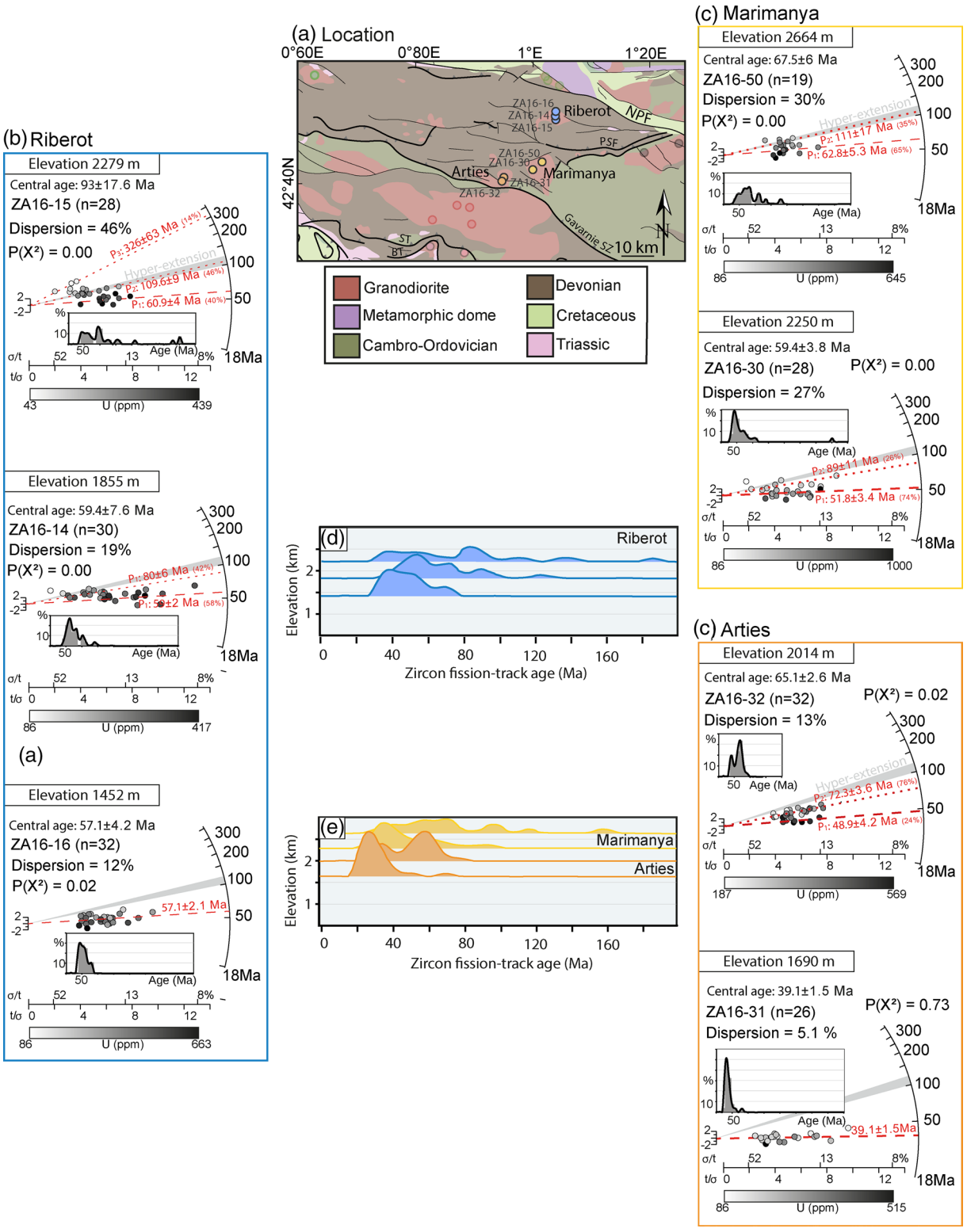

Figure 8. Detailed ZFT records of Gavarnie unit (Radial plot & density plot obtained by Radialplotter software): (a) Location of ZFT samples, plutonic massifs and major structures (BT: Bono thrust; NPF: North Pyrenean Fault; PSF: Port Salau Fault; ST: Senet thrust). (b), (c) Radialplots including the Cretaceous hyper-extensional phase (*light gray*) and (d)–(e) Age density plot versus Elevation for Riberot, Marimanya, and Arties massif (in light *blue*, *yellow* and *orange*, respectively).

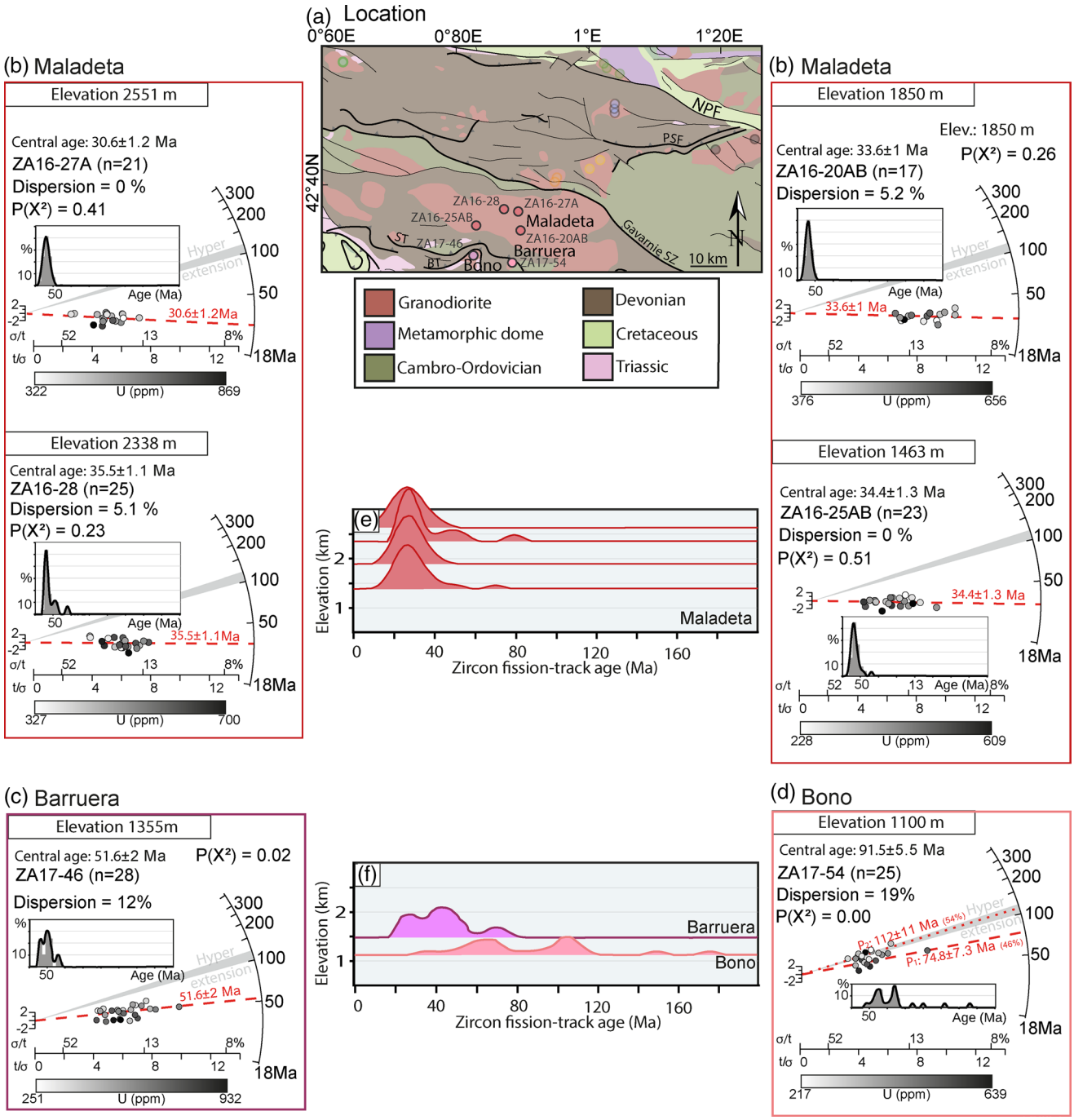

Figure 9. Detailed ZFT records for the southern massifs of the Orri unit (radial plot & density plot obtained by Radialplotter software): (a) location of ZFT samples, plutonic massifs and major structures (BT: Bono thrust; NPF: North Pyrenean Fault; PSF: Port Salau Fault; ST: Senet thrust). (b, c, and d) Radial plots including the Cretaceous hyper-extensional phase (*light gray*). (e) and (f) Age density plot versus Elevation for Maladeta, Barruera, and Bono massif (in *red*, *purple,* and *pink*, respectively).

between 110 and 70-60 Ma. This stage is followed by faster cooling at ca. 10°C/Myr from 60 to 50 Ma, and then slower cooling below 5°C/Myr. Modeling of the Riberot massif (Figure 12g) shows two cooling stages: (i) cooling at a rate of ~7°C/Myr from ca. 70 to 40 Ma, and (ii) slower cooling at a rate of ~ 1°C/Myr, after 40 Ma. The Marimanya and Arties massifs (Figure 12h) t-T path is defined by constant cooling at ca. 7°–8°C/Myr since ca. 50 Ma. Around 25 Ma, the massif reached near surface temperatures and slowly cooled at a

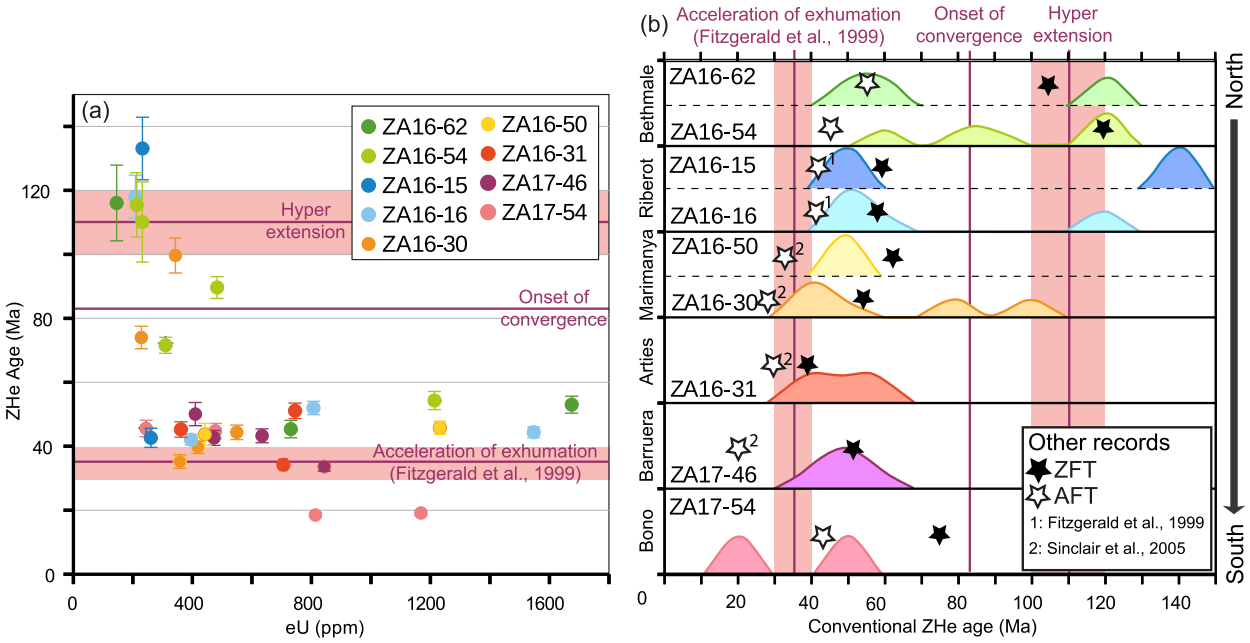

Figure 10. Zircon (U-Th)/He ages: (a) ZHe ages versus effective uranium content (eU = U + 0.235 Th); (b) vertical profiles of ZHe density plot in each pluton from north to south plotted with published deformational events and average AFT age (*white* star) and youngest population (P_1) of ZFT age (*black* star) from this study (added to previous work from Fitzgerald et al., 1999; Sinclair et al., 2005).

rate of ca. 2°C/Myr. The Maladeta massif (Figure 12i) reached temperatures of 300°C around 39 Ma, and the cooling rate could be estimated at ca. 39–30°C/Myr until ca. 32 Ma. Finally, the cooling rate decreased to lower values also observed in the northern plutons (~2°C/Myr). The cooling of the Barruera massif (Figure 12j) began at around 50 Ma at a rate of ~8°C/Myr until 40 Ma, before slowing down to a steady rate estimated at ~ 2°C/Myr (close to cooling rates of the Bethmale massif during early collision). QTQt modeling suggests an increase of cooling rate at ca. 8 Ma to a rate of around 9°C/Myr.

6. Discussion

6.1. ZFT Age-eU and ZHe Age-eU Relationships

The ZFT closure temperature not only depends on cooling rate but also on the amount of accumulated radiation damage in zircon, which is influenced by its uranium content (Bernet & Garver, 2005; Rahn et al., 2004). In this study, zircon is from 300 Ma Variscan plutonic massifs. Therefore, they accumulated significant radiation damages and probably have fission-track closure temperatures of ca. 240°C ± 20°C for an orogenic cooling rate of 15°C/Myr (Bernet, 2009; Brandon et al., 1998). However, as described previously, many samples show a spread of individual zircon ages defining several ZFT peak ages (Figures 7c and 8b, c, 9d). Such a dispersion of single grain ages reflects partial annealing that may indicate different diffusion kinetics related to variations of the original uranium content: the higher the uranium content, the younger the age. Grains with higher amounts of radiation damages have lower closer temperatures and therefore are more sensitive to partial annealing, hence these grains have younger apparent ZFT cooling ages.

In the AZ, several samples present mid-Cretaceous ZFT ages (Bethmale and Borderes-Louron samples, Figure 7). In these northernmost samples, only one ZFT grain-age population is identified. The dispersion is rather low, especially in the low-elevation samples. Therefore, these ages are most likely fully reset and therefore considered as true cooling ages. Further south, multiple ZFT age populations are observed in samples collected at elevations above 1,450 m, in Riberot and above 1,700 m in Marimanya-Arties massifs. The break in slope mostly observed in Riberot (slightly in Marimanya-Arties) tends to suggest an exhumed partial annealing zone exposed at 1,700–2,000 m elevation in the Gavarnie unit (Figures 11b). In samples at

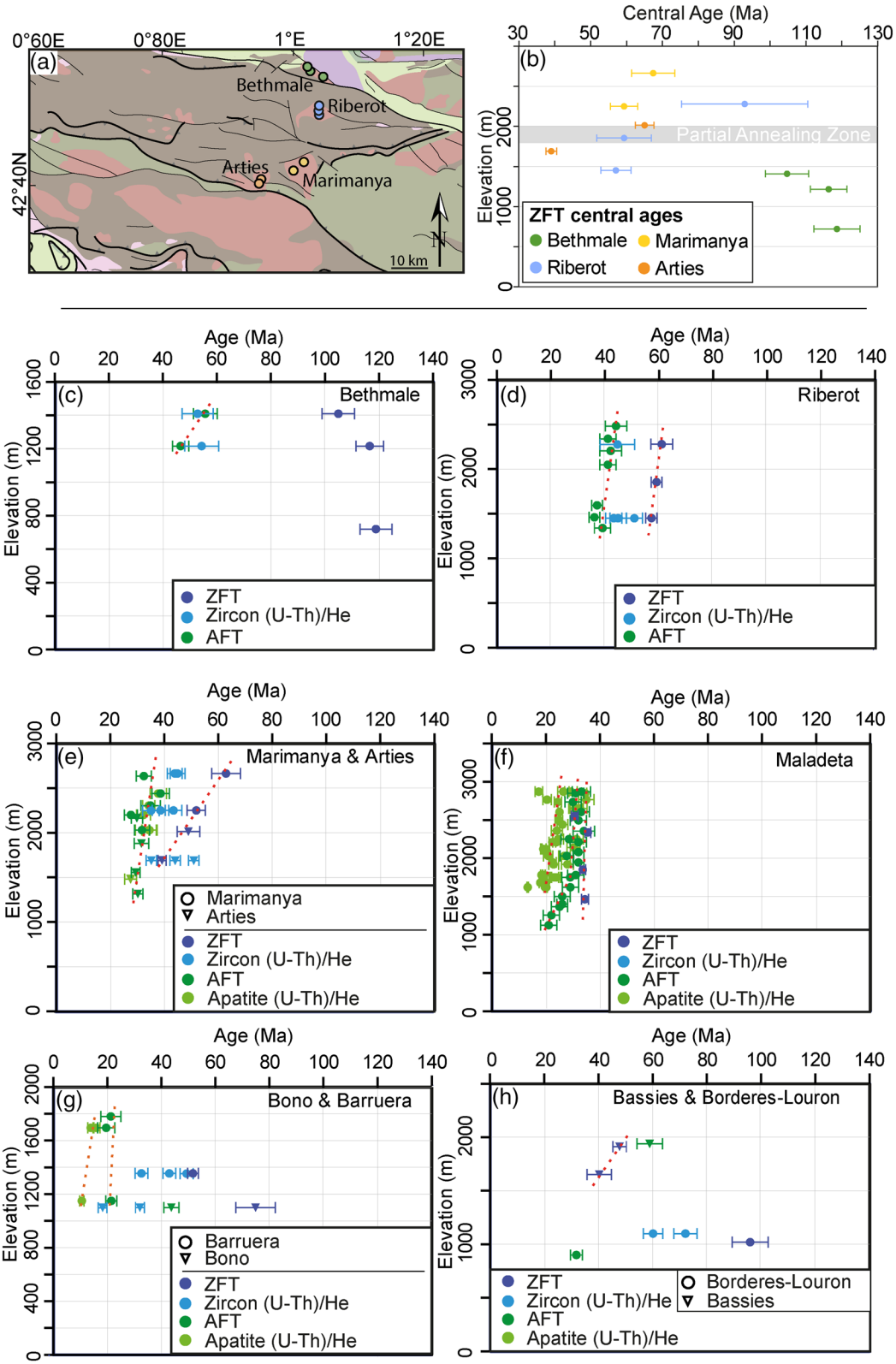
(a)
0°60E
0°80E
1°E
1°20E
42°40N
Bethmale
Riberot
Arties
Marimanya
N
10 km
(b)
Central Age (Ma)
Elevation (m)
Partial Annealing Zone
ZFT central ages
Bethmale
Marimanya
Riberot
Arties
(c)
Bethmale
(d)
Riberot
(e)
Marimanya & Arties
Marimanya
Arties
(f)
Maladeta
(g)
Bono & Barruera
Barruera
Bono
(h)
Bassies & Borderes-Louron
Borderes-Louron
Bassies
Age (Ma)
Elevation (m)
ZFT
Zircon (U-Th)/He
AFT
Apatite (U-Th)/He

high elevation from the Riberot and the Marimanya massif (Figure 8), but also in the Bono and the Bassies massifs (Figures 7c and 9d, respectively), one population is mid-Cretaceous in age. As mentioned above, these older zircons usually correspond to relatively low uranium contents of around 200 ppm.

There exists also a potential control of radiation damage on the ZHe ages, as pointed out and calibrated by Guenthner et al. (2013). In our data set, this could explain the spread of ages for individual samples from mid-Cretaceous to Eocene, which describes a global negative correlation with eU on Figure 10a. In such a framework, the oldest ZHe ages (~200 ppm eU) would correspond to the highest closure temperatures, whereas the youngest ones (>400 ppm eU) would correspond to lower closure temperature. The good correspondence of these old and young ZHe age populations with ZFT and AFT ages respectively, suggest that associated closure temperatures range from ~200°C to ~110°C. Additionally, in agreement with fission-track data, only the northern massifs (Bethmale, Riberot, Marimanya) record the old mid-Cretaceous population, whereas the southern one exhibit ages younger than 60 Ma. Even if such a framework is supported by a negative ZHe age versus eU correlation (Figure 10a) in agreement with theoretical model, the QTQt inversions where not able to reproduce such old populations (Figure 12). Recently, the calibration of the radiation damages dependent model of Guenthner et al. (2013) implemented in QTQt and HeFTy has been called into question by some studies (Gautheron et al., 2020; Vacherat et al., 2016). Gautheron et al. (2020) investigated this potentiality using ZHe data published for Variscan granites from the Pyrenean range (V. Bosch et al., 2016; Vacherat et al., 2016) and proposed that the actual maximum He retentivity (between positive and negative correlations in the diffusion vs. alpha dose space) does not occur at 2×10^{18} alpha/g (as proposed by the Guenthner et al., 2013 model) but significantly lower between 2 and 5×10^{17} alpha/g, close to the no-chain alpha recoil percolation level calculated by Ketcham et al. (2013). Such a potential calibration offset could trigger inability of QTQt to reproduce correctly the full range of ZHe ages in the damage dependent multichronometric framework, especially for the older population which would correspond to this maximum of retentivity. Despite our current ability to model correctly the He diffusivity and its dependence to damages, we do consider ZHe data from Pyrenean massifs since they are in quite good agreement with other thermochronometers and quarry a multi-chronological message.

6.2. Alpine Deformation in the Axial Zone

6.2.1. Exhumation

The dataset of this study first provides new constraints on the syn-rift thermal evolution of the AZ. The northernmost Gavarnie unit (such as Bethmale massif) started to cool during mid-Cretaceous times (Figure 13). The age of 110 Ma is probably too old for post-rift thermal relaxation. Thus, cooling is most likely due to denudation as the AZ probably corresponded to the southern rift shoulder. Moreover, during mid-Cretaceous times, in the northern AZ, the geothermal gradient was most likely high as suggested in Bellahsen et al. (2019). In the northern AZ, outcrops of Triassic beds (Figure 4) indicate that the paleo-burial of the northernmost massifs such as the Bethmale or Riberot was equivalent to the thickness of Mesozoic series (i.e., few km). Given all the uncertainties, considering that the northern AZ was the footwall of the extensional detachment (now NPF), a ZFT closure temperature around 240°C ± 50°C, and a paleo-burial depth estimated at about 5 ± 1 km (probably less), it appears that the geothermal gradient was higher than normal, possibly around at least 50 ± 20°C/km.

The oldest ZFT and ZHe age populations were probably affected by pre-orogenic events (>83 Ma, Figures 7–10). In the Riberot massif (Figure 8b, 2,279 m), one sample provided a ZFT age population of around 323 ± 63 Ma, which most probably represents a magmatic age. On the contrary, the youngest age populations, usually from Paleocene to Oligocene, are mainly observed in samples with higher uranium contents. These

Figure 11. Age-elevation diagrams from apatite fission-track (AFT), zircon fission-track (ZFT), apatite (U-Th)/He (AHe), and zircon (U-Th)/He (ZHe). (a) Location of samples; (b) central age versus elevation of samples from each massif in the Gavarnie unit; (c) youngest peak age versus elevation for the Bethmale massif; (d) youngest peak age versus elevation for the Riberot massif; (e) youngest peak age versus elevation for the Marimanya and Arties massifs; (f) youngest peak age versus elevation for the Maladeta massif; (g) youngest peak age versus elevation for the Bono and Barruera massifs; (h) youngest peak age versus elevation for the Bassies and Bordères-Louron massifs. Estimated exhumation rates were obtained thanks to the least square method on thermochronological data (*Red* dashed lines) and their associated error bars were calculated manually according to standard error of those data. Age data are compiled from this study and Fitzgerald et al. (1999), Sinclair et al. (2005), Gibson et al. (2007), see Table S4.

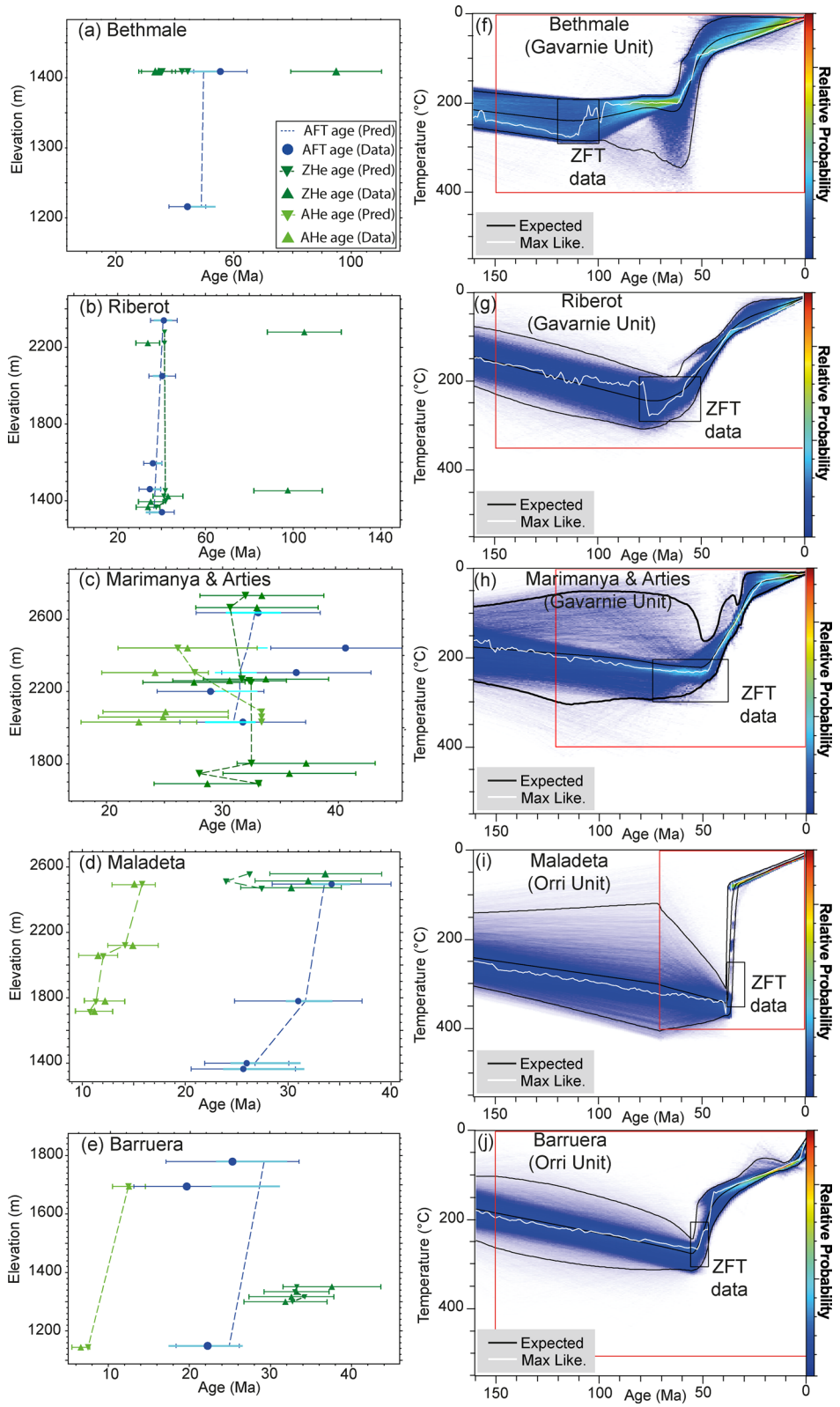
(a) Bethmale
(b) Riberot
(c) Marimanya & Arties
(d) Maladeta
(e) Barruera
Elevation (m)
Age (Ma)
AFT age (Pred)
AFT age (Data)
ZHe age (Pred)
ZHe age (Data)
AHe age (Pred)
AHe age (Data)
(f) Bethmale (Gavarnie Unit)
(g) Riberot (Gavarnie Unit)
(h) Marimanya & Arties (Gavarnie Unit)
(i) Maladeta (Orri Unit)
(j) Barruera (Orri Unit)
ZFT data
Expected
Max Like.
Temperature (°C)
Relative Probability

younger ages are interpreted as being related to Alpine exhumation/cooling. The new thermochronological dataset and t-T models also permit to discuss the initiation (Figure 13) and the spatio-temporal variation of exhumation (Figure 14a). Previously, the onset of Alpine denudation in the AZ was constrained around 50 Ma mainly by AFT data (Fitzgerald et al., 1999; Garwin, 1985; Gibson et al., 2007; Jolivet et al., 2007; Maurel, 2003; Maurel et al., 2008; Metcalf et al., 2009; Sinclair et al., 2005; Yelland, 1991). Indirectly, detrital ZFT indicated Cretaceous denudation, possibly in the eastern AZ (Whitchurch et al., 2011).

Our new ZFT ages document a first orogenic phase dated at 65 Ma in the AZ (Figure 13). Therefore, they suggest a complex sequence of shortening/exhumation, most likely more complex than in previous published models (e.g., Sinclair et al., 2005). We propose that the onset of cooling started around 65 Ma in the northernmost massif (Bethmale) as well as further south (Riberot), and around at least 50 Ma in the southern massifs (Marimanya, Arties and Barruera) (Figure 14a). In the southernmost massif (Bono) exhumation is older, ca. 75–70 Ma (Figure 13). These data suggest a possible exhumation of the whole AZ at around 75–65 Ma. Neglecting the ZFT ages in the Bono massif would suggest a slow southward propagation of the initiation of slow exhumation during Paleocene and Eocene times. Thus, even if a sequence can be deciphered, we propose that exhumation was rather distributed because: exhumation was slow, possibly already active since 70 Ma in the southermost AZ, and may have started even earlier in the Marimanya, Arties and Barruera massifs as ZFT ages (or thermochronological ages in general) do not necessarily record the onset of exhumation if they originate from deep initial levels (Figure 14a). Such distributed exhumation is most likely due to distributed shortening. This is also supported by several late Cretaceous to ca. mid-Eocene shear zones within the AZ (Figure 3; Airaghi et al., 2020; A. M. McCaig & Miller, 1986; Wayne & McCaig, 1998).

From 70 to 40 Ma, thermochronological ages indicate some significant cooling (Figures 8d–8e, 9f), questioning the Paleocene quiescence phase dated from ca. 68 to 56 Ma, inferred on the base of tectono-sedimentological data from the northern and southern parts of the Pyrenees (Boer et al., 1991; Grool et al., 2018; Whitchurch et al., 2011) and kinematic studies (e.g., Rosenbaum et al., 2002). However, thermochronological models may not capture such short event. In any case, a distributed exhumation in the AZ during Paleocene times, that is, not linked to any thrust in the frontal parts/basins, may have no tectono-sedimentary effect and could be recorded as a quiescence phase in the basins. Inverse thermal modeling tends to confirm rapid cooling, hence rapid exhumation during late Eocene-Oligocene times. However, our new results show that such acceleration concerns only the Maladeta massif (Figure 14a). In all other massifs, our data and modeling indicate lower exhumation rates, as low as during Paleocene-Eocene times.

6.2.2. Shortening

From a structural point of view, our cross section and its restoration is different from both the "classical" models (e.g., Mouthereau et al., 2014; Muñoz et al., 1992; Roure et al., 1989) and more recent publications (e.g., Cochelin et al., 2018). The main differences between these published cross-sections are: (i) the amount of Alpine shortening accommodated in the AZ varies from ca. 71 to 111 km in most models (Erdős et al., 2014; Espurt et al., 2019; Grool et al., 2018; Mouthereau et al., 2014; Teixell et al., 2018) and is extremely limited (~30 km) in recent publications (Cochelin et al., 2018); and (ii) the amplitude of tilting on the Gavarnie unit which is large in the classical antiformal stack and limited according to recent results (Cochelin et al., 2018).

Our alternative section presents only limited tilting in the AZ (Figure 4b). To verticalize the NPF we propose the existence of top-to-north shear zones at depth (Figure 15), for which we have documented some evidence at smaller scale in the field (Figures 5 and 6). This results in less-pronounced antiformal stacking compared to the classical models (Figure 15). The total amount of Alpine shortening in the AZ is similar

Figure 12. Thermal inversion performed with QTQt software. Apatite (U-Th)/He (AHe) and apatite/zircon fission-track (AFT and ZFT, respectively) data predictions (Pred) from QTQt inversion models are compared to the available thermochronological dataset (Data) in the following massifs: (a) Bethmale; (b) Riberot; (c) Marimanya-Arties; (d) Maladeta; (e) Barruera. Time-temperature histories from QTQt inversion of thermochronological data (AFT, AHe, ZHe) along the ECORS-Toulouse profile are represented in the following massifs: (f) Bethmale; (g) Riberot; (h) Marimanya-Arties; (i) Maladeta; (j) Barruera. The plot of inverse models includes the expected model (weighted mean model: *black*), the maximum likelihood model (model with the best data fit: *white*) and the range for general prior (*red*).

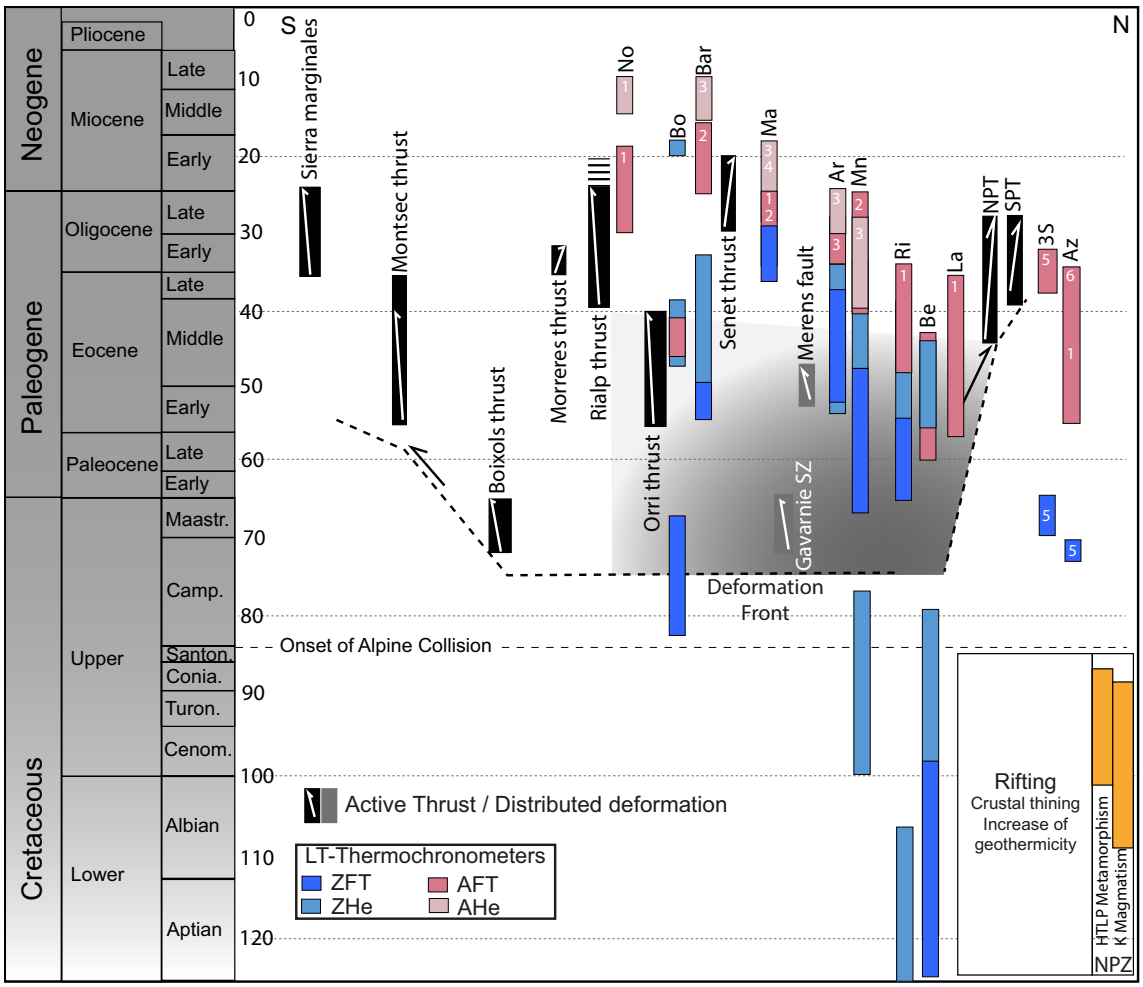

Figure 13. Synthesis of Mesozoic and Cenozoic events in the Pyrenees, based on thermochronological constraints from this study and Fitzgerald et al. (1999), Gibson et al. (2007), Metcalf et al. (2009), Morris et al. (1998), Sinclair et al. (2005), and Yelland (1991). Thrust activity and basin constrains from Beamud et al. (2011), Bond and McClay (1995), Deramond et al. (1993), Erdős et al. (2014), Filleaudeau et al. (2011), Labaume et al. (1985), Meigs et al. (1996), Meigs and Burbank (1997), Mouthereau et al. (2014), Puigdefàbregas and Souquet (1986), Rahl et al. (2011), and Whitchurch et al. (2011).

to that inferred by Mouthereau et al. (2014), as a significant crustal root and exhumation are documented. However, the thermochronological evidence of regionally distributed cooling/exhumation (recorded since 75-70 Ma on both borders of the AZ), in addition to the distributed reverse shear zones observed in the field (Figures 5 and 6), suggests a higher amount of distributed shortening in the AZ, most likely during early orogenic stages. To be consistent with the previous estimation of Alpine shortening in the central AZ (Mouthereau et al., 2014), we propose that, along the ECORS profile, the so-called Gavarnie thrust may be a shear zone accommodating about 5 km of shortening (linked to the shortening on the Boixols thrust estimated by Bond & McClay, 1995); thus, much less than previously proposed, except by Soler et al. (1998). This structure zone also called the Estarón shear zone is the overhanging, southern limb of the Pallaresa anticline (Figure 4).

6.3. Sequential Restoration

The shortening sequence constrained by literature data (Figure 2), by our new thermochronological data, and inverse thermal modeling is presented in Figure 15. The trace of the section strikes through the plutonic massifs and it is located only few km west of the ECORS profile. Present-day structures at depth are reconstructed considering the most recent geophysical data (Chevrot et al., 2018).

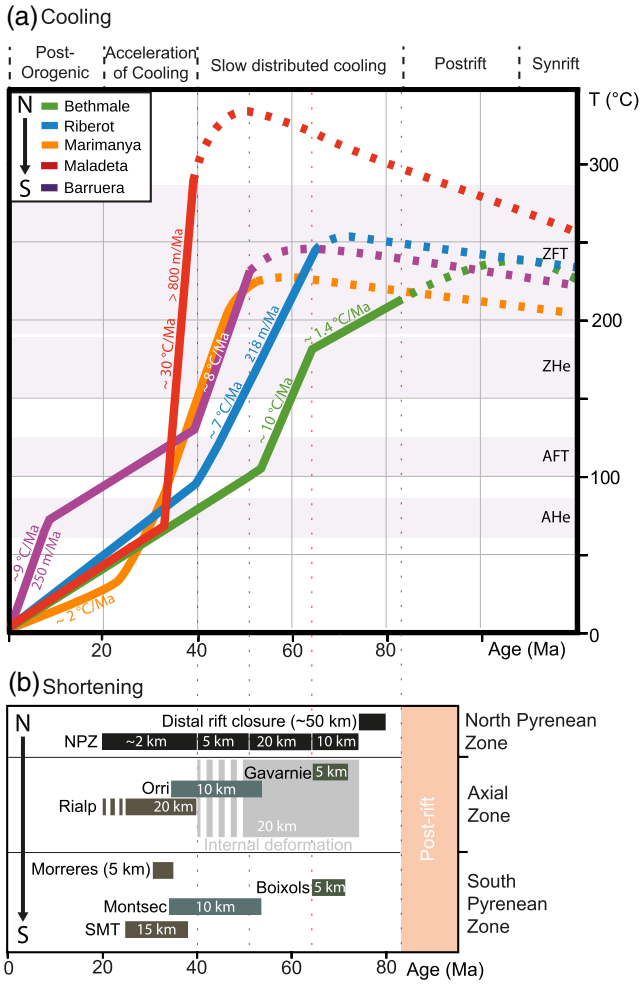

Figure 14. Thermal evolution and shortening sequence. (a) Thermal evolution based on results of inverse modeling in Axial Zone, Pyrenees. Dashed lines correspond to t-T path not constrained by inverted thermochronological data; (b) thrust and shortening sequence in North Pyrenean Zone, Axial Zone and South Pyrenean Zone (Colors highlight linked thrusts). BT: Bono thrust; MT: Montsec thrust; BxT: Bóixols thrust; OT: Orri thrust; GT: Gavarnie thrust; Be: Bethmale; Bl: Bordères-Louron; R: Riberot; Mn: Marimanya; A: Arties; Ma: Maladeta; Br: Barruera.

Total shortening estimates during Alpine collision vary from the western to the eastern Pyrenean transect (Figure 1b): 75–80 km in the western part along ECORS-Arzacq profile (Teixell, 1998), 71 km (plus 56 km involving the closure of NPZ rift) along Nestes-Cinca transect (Espurt et al., 2019; Teixell et al., 2018), 92 km (plus ~ 50 km of subducting distal domain before initiation of collision) along the ECORS-Pyrenees profile (Mouthereau et al., 2014), 111 km of shortening through eastern Pyrenees (Grool et al., 2018). The total shortening estimated in Figure 15 is based on Mouthereau et al. (2014). As mentioned above, the partitioning between the NPZ, the AZ, and the SPZ and between localized and distributed shortening is re-evaluated considering our new low-temperature thermochronological constraints.

The sequential restoration (Figure 15) based on published and newly acquired thermochronological data consists of 4 distinct phases from 84 Ma to present-day: (i) from 84 to 71 Ma (post rift and subduction of exhumed mantle), (ii) between 71 and 40 Ma (distributed crustal shortening and mainly distributed, slow exhumation), (iii) from 40 to 20 Ma (underplating of the Rialp unit, localized shortening, and strong exhumation as shown in the Maladeta massif), (iv) since 20 Ma (post-orogenic evolution). This sequence thus includes two phases of collision s.s.: an early distributed phase of shortening between 71 and 40 Ma and a localized one between 40 and 20 Ma. For each restored step, a pin line is fixed at the northern limit of the non-deformed European crust (Figure 15) and the total length of strata and surface of the crust is preserved. Each of these phases is described in detail below.

6.3.1. Pre-collisional Phase

The first stage of convergence is associated with subduction of exhumed mantle and closure of the Cretaceous Rift (from 84 to 72 Ma). The amount of shortening accommodated during this time interval has been estimated to around 50 km, based on the difference between the total amount of Iberian-European plate convergence to be accommodated and the restored section at 72 Ma (Mouthereau et al., 2014). Furthermore, during the same period, cooling of abnormally hot basins in the NPZ, originally located on hyper-extended crust of the European margin, occurred. In the AZ, partial resetting of ZFT recorded in the Gavarnie unit and the very slow cooling of the Bethmale massif (~1.4°C/Myr; Figure 12f), and possibly the Bono massif (Figure 13), may be consistent with syn-rifting denudation of the northern AZ. This stage could also have been followed by a post-rift thermal relaxation. As explained above, the oldest ZFT and ZHe populations and the low burial of plutons (Figure 13) support a high geothermal gradient inherited from Cretaceous rifting in the NPZ and AZ. Moreover, this thermal state in AZ may have persisted during early Alpine collision times as suggested for NPZ (Vacherat et al., 2016).

6.3.2. Early Collision: Slow and Distributed Paleocene-Eocene Exhumation

From 72 to 65 Ma, the onset of tectonic inversion mostly took place along the Bóixols thrust in the SPZ, as dated and constrained by growth strata in upper Campanian sandstones and $^{39}Ar/^{40}Ar$ dating (Bond & McClay, 1995; Rahl et al., 2011). The amount of shortening accommodated by this structure corresponds to about 5 km (Bond & McClay, 1995). During early collision, the Gavarnie shear zone corresponds to the prolongation of Bóixols thrust at depth (Figure 15). Thus, in our restoration, this shortening value has been attributed to the Gavarnie shear zone (inverted southern limb of the Pallaresa anticline). The rest

10.1029/2020TC006614

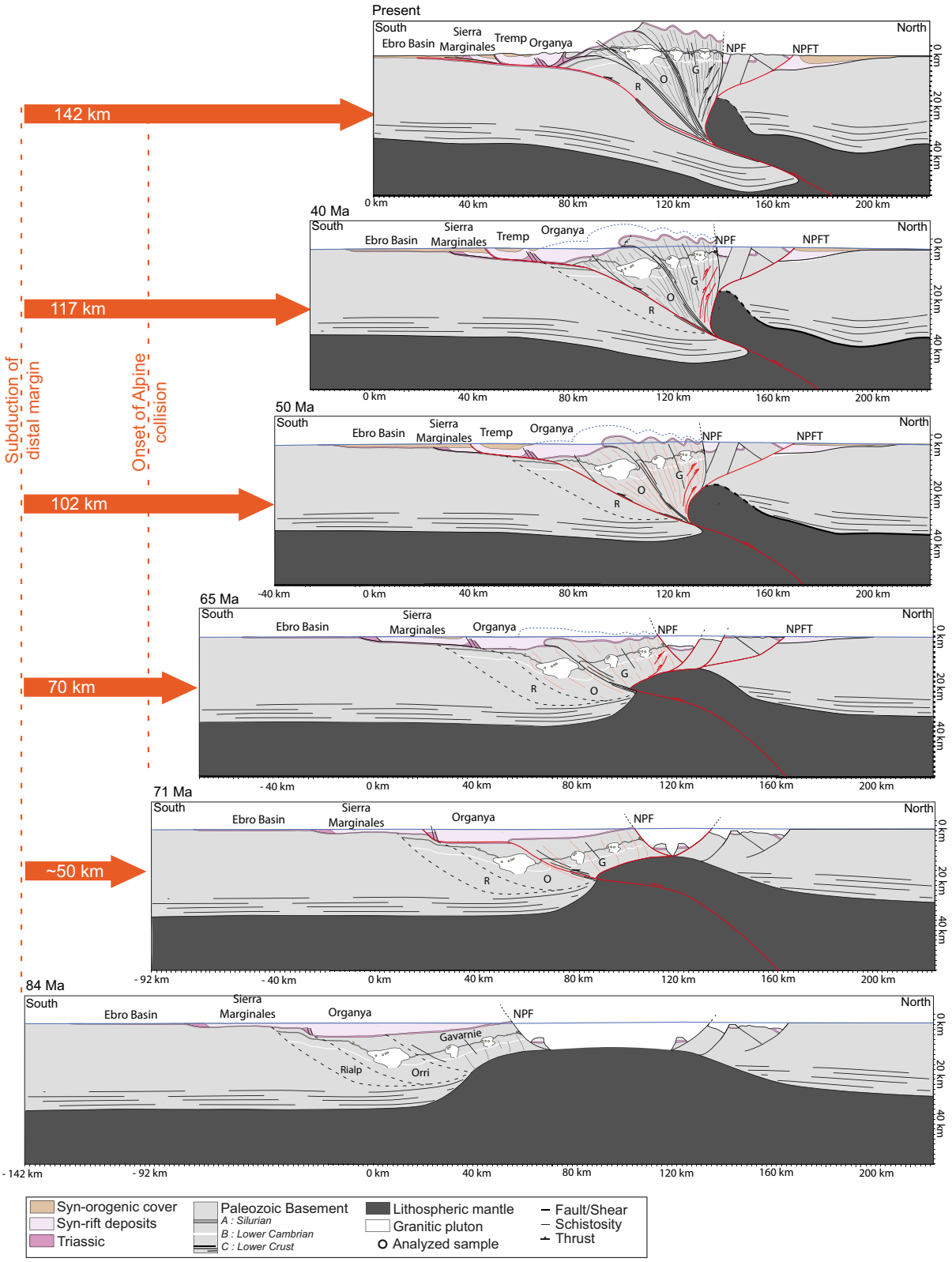

Figure 15. Sequential restoration of the central Pyrenees (ECORS-Pyrenees profile) from 84 Ma to present day. The deep crustal structure is based on Choukroune & the ECORS-Pyrenees team (1989) and Chevrot et al. (2018). Basins thickness reconstruction and shortening sequence are modified from Mouthereau et al (2014). O: Orri; G: Gavarnie; R: Rialp; NPF: North Pyrenean Fault; NPFT: North Pyrenean Frontal thrust.

of the shortening (5 km) estimated in Mouthereau et al. (2014) has been distributed, because no other major, discrete observed structure may have accommodated this shortening in the area. This shortening may explain cooling, hence exhumation of rocks taking place in the 72-65 Ma interval in the Bethmale Massif (Figure 14), in addition to partially reset ZFT ages in most of the studied massifs (Riberot, Bethmale). During this shortening event, no clear evidence for large displacement can be reported in the Gavarnie shear zone (Cochelin et al., 2018). However, such large displacement is invoked by Metcalf et al. (2009) to explain a possible Cenozoic significant heating of the Maladeta pluton. However, such heating is mainly based on Triassic rocks in the Gavarnie footwall whose structural relationships with the Maladeta basement are unclear in the field. Thus, we alternatively suggest only a slight burial of the Maladeta massif. During this time interval, 10 km of shortening in the NPZ is also taken into account (Mouthereau et al., 2014).

As mentioned above, the northern AZ (i.e. future Gavarnie unit) has not been significantly tilted after the formation of its Alpine schistosity (Cochelin et al., 2018). However, the NPF is considered as an inherited extensional detachment which was verticalized during Pyrenean orogenesis (Cochelin et al., 2018; Deramond et al., 1984; McCaig et al., 1986). As a consequence, deep top-to-the-north shear zones are deducted from small analogue outcropping structures (Figure 5) for the northernmost part of the AZ and most likely verticalized the NPF (Figure 15).

Between 65 and 50 Ma (Figure 14a), Late Cretaceous slow cooling rates recorded in the northern Gavarnie unit (e.g. Bethmale and Riberot) increased to ~ 5°C–10°C/Myr (Figures 12f and 12g), with an exhumation rate of around 200 ± 50 m/Myr (Figure 14a). Contrary to published thermochronological dataset and tectonic restorations (Mouthereau et al., 2014; Muñoz et al., 1992; Roure et al., 1989), early Eocene ZFT ages are observed both in southern Gavarnie unit (e.g., Arties; Figure 8e) and in southern AZ (e.g. Barruera massif; Figure 9f).

The thermochronological data in the southernmost (Bono massif; Figure 9d) and the northernmost (Bethmale massif; Figure 7b) massifs suggest a coeval onset of cooling, and therefore support early Alpine cooling distributed through the whole AZ. This continuous cooling observed on the whole ECORS-Pyrenees profile does not support a Paleocene tectonic quiescence as documented in several studies using other types of constraints (Boer et al., 1991; Grool et al., 2018; Rosenbaum et al., 2002; Whitchurch et al., 2011). The amount of shortening associated with distributed deformation in this early phase from 65 to 50 Ma was estimated to be around 10 km by comparing: (i) the total shortening from previous tectonic restorations (Mouthereau et al., 2014) and (ii) the estimated shortening localized along coeval thrusts in the southern basins. During the same period in the NPZ, inverse thermal modeling of AFT data suggests a steady state cooling since 70 Ma, which is associated with 20-km shortening (Mouthereau et al., 2014).

Cooling of the Bethmale massif slowed down below 2°C/Myr at around 55–50 Ma in the northern AZ, as constrained by QTQt modeling (Figures 14a and 11c), while the northern-central massifs in the Gavarnie unit (Riberot, Marimanya and Arties) were still cooling at constant rate. The cooling rate of the Orri unit (Barruera massif) at around 55 Ma is similar to the ones assessed in northern massifs (~8°C/Myr). At the same period, the Montsec thrust, rooted in the Orri thrust, accommodated about 13 km of shortening from ca. 55 to 40 Ma in the SPZ (Figure 15; Meigs et al., 1996). However, it should be noted that the partially reset ZFT data from the southernmost pluton of the Orri unit (Bono) suggests that cooling already initiated at about 70 Ma (Figure 9d). Between 50 and 40 Ma distributed shortening was estimated to around 4 km in the AZ, for a total shortening of ca. 15 km according to restoration in Mouthereau et al. (2014). At the same time, deformation was localized on the NPFT ramp in the NPZ (Mouthereau et al., 2014; Vacherat et al., 2016).

As shown on Figure 14a, the models suggest a complex cooling sequence that may have been distributed through the whole AZ during Paleocene and Eocene times. Reverse top-to-the-south shear zones have been dated to around 50 Ma such as Merens shear zone (A. M. McCaig & Miller, 1986), Neouvielle shear zones (Wayne & McCaig, 1998) and Bielsa shear zones (Airaghi et al., 2020) suggesting that their activity induced a distributed exhumation, hence cooling of the AZ as developed above. To sum up, in the AZ, the complex cooling sequence (Figure 14a) observed during this first orogenic stage (70–40 Ma) includes distributed

slow cooling and exhumation which may be interpreted as due to a distributed shortening. A slight acceleration and the migration of exhumation toward the south around 50 Ma and the activation of the Orri thrust suggest that the 50-40 Ma period represents a transition between distributed and localized shortening (Figures 14a and 14b.

6.3.3. Late Collision: Fast Rapid Local Late Eocene-Oligocene Localized Exhumation

From ca. 40 to 32 Ma about 5 km shortening was estimated in the NPZ by balancing folded structures (Lavelanet and Mas d'Azil anticlines) related to a decrease in bedding dips near the early Oligocene Palassou Formation (Mouthereau et al., 2014). The shortening is also accommodated by the verticalization of the NPF (see previous section and Figure 15). The amount of shortening taking place at around 37 Ma in the SPZ was localized in the SMT and the MBT, and inferred to accommodate ca. 15 and 5 km of displacement (Meigs et al., 1996), respectively. This shortening is attributed to displacement along the Rialp ramp in the AZ (Figure 14b).

Between 40 and 32 Ma in the AZ, a relatively high cooling/exhumation rate is only recorded in the central Maladeta massif (Figure 14a). Our inverse thermal modeling (Figure 14) shows fast cooling (~30°C/Myr) related to exhumation of at least 800 m/Myr and up to 2–3 km/Myr (according to Fitzgerald et al., 1999). As shown above, this orogenic cooling is coeval with shortening on the Rialp ramp (Figure 14b). The Rialp ramp can thus be located just under the Maladeta massif and exhumation is therefore spatio-temporally associated with the underplating of the Rialp unit. In the external part, this exhumation phase is also confirmed by detrital ZFT records from the south-central basins, suggesting accelerating erosion in the AZ since the late Priabonian around 37–35 Ma (Fitzgerald et al., 1999; Metcalf et al., 2009; Whitchurch et al., 2011).

Our dataset also shows for the first time that the other massifs in the AZ (e.g. Bethmale, Riberot and Barruera massifs) experienced slow cooling rates (less than 2°C/Myr) simultaneously at ca. 40–20 Ma, suggesting only limited shortening and the cessation of distributed shortening (Figure 14a) that was replaced by localized shortening on the Rialp thrust. Thus, localization led to fast exhumation centered on the Maladeta massif just above the ramp (Figure 14b).

Furthermore, granitic pebbles with 65 Ma ZFT ages were observed in the Oligocene Sis conglomerates (Beamud et al., 2011). This suggests that some plutonic massifs were exhumed to the surface at the onset of collision, approximately at 40 Ma. According to our reconstruction (Figure 15), we can consider that the northernmost plutonic massifs of the AZ (such as Bethmale) could have reached the surface during this period.

6.3.4. Post-Orogenic Cooling/Exhumation

The later significant decrease of cooling rates in our exhumation sequence (Figure 14) is interpreted as the transition from an orogenic to a post-orogenic state. In the Gavarnie unit, the onset of such low rates is observed from at least 40 Ma (Riberot) to 25 Ma (Marimanya-Arties). Whereas in the Barruera massif, modeling using the finite-element code "Pecube" of AFT/AHe data (Gibson et al., 2007) suggests post-orogenic exhumation since 19 Ma, followed by gradually decreasing exhumation rates. This interpretation is consistent with the youngest activity of the SMT inferred to have taken place at around 24.7 Ma (Meigs et al., 1996). Thus, the onset of post-orogenic exhumation is not clearly constrained in the AZ, but most likely around 20 Ma (Gibson et al., 2007; Mouthereau et al., 2014). However, AFT modeling of the Maladeta massif supports post-orogenic exhumation at 10–5 Ma (Fitzgerald et al., 1999), which is in good agreement with our QTQt modeling results of the Barruera data (Figure 12j). Considering literature and the low cooling rates (~2°C/Ma) recorded by each model since at least 25 Ma (Figures 12 and 14), we here suggest that the AZ entered the post-orogenic phase at ca. 20 Ma (Gibson et al., 2007; Mouthereau et al., 2014) before it experienced post-orogenic exhumation from 10 to 5 Ma (Fitzgerald et al., 1999). Post-orogenic extension possibly driven by contrasting crustal thickness and densities, inherited from Mesozoic rifting, has been proposed for last 10 Ma exhumation in the western Pyrenees (Fillon et al., 2020).

6.4. Insights Into the Early Growth of Orogenic Wedges

These new data show that the early collisional phase, following the period of resorption/subduction of oceanic or exhumed mantle domains, is characterized by distributed exhumation and shortening. Such distributed shortening is characterized by Alpine penetrative schistosity and several shear zones active throughout the AZ accommodating only small amounts of displacement. Such result suggests that the northern AZ is characterized by an overall pure shear Alpine deformation, i.e. a N-S shortening and vertical stretching. Such a model is supported by Cenozoic ages of some shear zones throughout the AZ and slow, distributed Eocene exhumation. However, the distributed exhumation could be confirmed by thorough widespread dating of deformation in the northern AZ.

Similar results were obtained in Europe through the western external Alps (e.g., Bellahsen et al., 2014), although with different kinematics, where Oligocene times are characterized by distributed shortening before the deformation localized along the frontal crustal ramps (Boutoux et al., 2016; Girault et al., 2020). The main difference with the Pyrenees is that, in the western external Alps, the shortening is accommodated by west-verging shear zones. However, in both cases, 10–30 km of distributed shortening were accommodated in the crustal wedge during time periods of about 10–30 Ma. Such distributed shortening may be explained by different factors. Feldspars were altered early during the crust evolution (Airaghi et al., 2020; Bellahsen et al., 2019). Thus, at the onset of Alpine shortening, they were seriticized and most likely very weak. As a consequence, the crust may have been weaker than normal and this widespread alteration may have caused distributed deformation. Inherited thermal weakening or syn-orogenic thermal weakening may also control distributed shortening by decreasing the overall crustal strength (Bellahsen et al., 2019). Finally, when shortening a passive margin, the switch between distributed to local modes of deformation may also be controlled by the transition between shortening of a significantly thinned crust and shortening of normal-thickness crust (see Figure 15). In any case, the occurrence of an early distributed shortening phase appears now as a common characteristic of the collisional wedge. It should be more systematically documented in different orogens, as it most likely contains key information on the mechanics of collisional wedges.

7. Conclusions

New LT thermochronological data from the Axial Zone provide insights into the evolution of the Pyrenean collisional wedge. During mid-Cretaceous times, the northern Axial Zone experienced high geothermal gradient and syn-rift denudation in relation with North Pyrenean Zone rifting. After a period possibly affected by thermal relaxation and early subduction of an exhumed mantle domain, a first phase of collision was characterized by relatively slow and distributed Paleocene-Eocene orogenic cooling through the whole Axial Zone from ca. 70 to 40 Ma interpreted as a distributed internal shortening. During this period, the Gavarnie shear zone was active but accommodated limited shortening. Between 50 and 40 Ma, a transitional period is characterized by both distributed and localized deformation on the Orri crustal ramp. A second phase of collision in the late Eocene-Oligocene is characterized by fast exhumation recorded in northern Orri unit, as shown by the Maladeta massif, and associated with the underplating of the Rialp unit. This contribution thus shows that collision in the Pyrenees started by significant distributed deformation/shortening from 70 to 40 Ma accommodating a total amount of shortening of at least 15 km. The mode of shortening is most probably controlled by thermal, and/or mineralogic weakening and structural inheritance. Only in a later stage it is followed by a phase of localized shortening with the activation of frontal crustal ramps in the proximal Iberian margin. Such a two-phase collision has been recognized in other orogens and may be characteristic of the evolution of orogenic wedges.

Data Availability Statement

Supporting information can be found at DOI (https://doi.org/10.6084/m9.figshare.12962435.v1) and includes: complete thermochronological dataset of central Axial Zone including fission-track data formatted for Radialplotter (Table S4), radial plots of AFT data of Bono and Bethmale massifs (Figure S1), additional time-temperature plots of un-modeled massifs (Figure S2), and an extended version of QTQt models including the initial constrain boxes (Figure S3).

Acknowledgments
This study is part of the Orogen program, a tri-partite research collaboration between CNRS, BRGM, and Total. The authors thank Bouchaïb Tibari for his precious help during data acquisition.

References

Airaghi, L., Bellahsen, N., Dubacq, B., Chew, D., Rosenberg, C., Janots, E., et al. (2020). Pre-orogenic upper crustal softening by lower greenschist facies metamorphic reactions in granites of the central Pyrenees. *Journal of Metamorphic Geology*, *38*, 183–204. https://doi.org/10.1111/jmg.12520

Albarède, F., Michard-Vitrac, A. (1978). Age and significance of the north pyrenean metamorphism. *Earth and Planetary Science Letters*, *40*, 327–332. https://doi.org/10.1016/0012-821X(78)90157-7

Beamud, E., Muñoz, J. A., Fitzgerald, P. G., Baldwin, S. L., Garcés, M., Cabrera, L., et al. (2011). Magnetostratigraphy and detrital apatite fission track thermochronology in syntectonic conglomerates: Constraints on the exhumation of the south-central pyrenees: South-central pyrenees magnetostratigraphy and thermochronology. *Basin Research*, *23*, 309–331. https://doi.org/10.1111/j.1365-2117.2010.00492.x

Beaumont, C., Muñoz, J. A., Hamilton, J., Fullsack, P. (2000). Factors controlling the Alpine evolution of the central Pyrenees inferred from a comparison of observations and geodynamical models. *Journal of Geophysical Research*, *105*, 8121–8145. https://doi.org/10.1029/1999JB900390

Bellahsen, N., Bayet, L., Denele, Y., Waldner, M., Airaghi, L., Rosenberg, C., et al. (2019). Shortening of the axial zone, pyrenees: Shortening sequence, upper crustal mylonites and crustal strength. *Tectonophysics*, *766*, 433–452. http://dx.doi.org/10.1016/j.tecto.2019.06.002

Bellahsen, N., Mouthereau, F., Boutoux, A., Lacombe, O., Jolivet, L., & Rolland, Y. (2014). Collision kinematics in the western external Alps: Kinematics of the Alpine collision. *Tectonics*, *33*, 1055–1088.

Bernet, M. (2009). A field-based estimate of the zircon fission-track closure temperature. *Chemical Geology*, *259*, 181–189. https://doi.org/10.1016/j.chemgeo.2008.10.043

Bernet, M., & Garver, J. L. (2005). Fission-track analysis of detrital zircon. *Reviews in Mineralogy and Geochemistry*, *58*, 205–237. https://doi.org/10.2138/rmg.2005.58.8

Boer, P. L., Pragt, J. S. J., & Oost, A. P. (1991). Vertically persistent sedimentary facies boundaries along growth anticlines and climate-controlled sedimentation in the thrust-sheet-top South Pyrenean Tremp-Graus Foreland Basin. *Basin Research*, *3*, 63–78. https://doi.org/10.1111/j.1365-2117.1991.tb00140.x

Bond, R. M. G., & McClay, K. R. (1995). Inversion of a Lower Cretaceous extensional basin, south central Pyrenees, Spain. *Geological Society, London, Special Publications*, *88*, 415–431. https://doi.org/10.1144/GSL.SP.1995.088.01.22

Bosch, G. V., Teixell, A., Jolivet, M., Labaume, P., Stockli, D., Domènech, M., et al. (2016). Timing of eocene–miocene thrust activity in the western axial zone and chaînons béarnais (west-central pyrenees) revealed by multi-method thermochronology. *Comptes Rendus Geoscience*, *348*, 246–256. https://doi.org/10.1016/j.crte.2016.01.001

Bouchez, J. L., & Gleizes, G. (1995). Two-stage deformation of the Mont-Louis-Andorra granite pluton (Variscan Pyrenees) inferred from magnetic susceptibility anisotropy. *Journal of the Geological Society*, *152*, 669–679. https://doi.org/10.1144/gsjgs.152.4.0669

Boulvais, P., Ruffet, G., Cornichet, J., & Mermet, M. (2007). Cretaceous albitization and dequartzification of hercynian peraluminous granite in the salvezines massif (French Pyrénées). *Lithos*, *93*, 89–106. https://doi.org/10.1016/j.lithos.2006.05.001

Boutoux, A., Bellahsen, N., Nanni, U., Pik, R., Verlaguet, A., Rolland, Y., et al. (2016). Thermal and structural evolution of the external western Alps: Insights from (U–Th–Sm)/He thermochronology and RSCM thermometry in the aiguilles rouges/mont blanc massifs. *Tectonophysics*, *683*, 109–123. https://doi.org/10.1016/j.tecto.2016.06.010

Brandon, M. T., Roden-Tice, M. K., & Garver, J. I. (1998). Late cenozoic exhumation of the cascadia accretionary wedge in the olympic mountains, northwest Washington state. *GSA Bulletin*, *110*, 985–1009. https://doi.org/10.1130/0016-7606(1998)110<0985:LCEOTC>2.3.CO;2

Cande, S. C., & Kent, D. V. (1992). A new geomagnetic polarity time scale for the Late Cretaceous and Cenozoic. *Journal of Geophysical Research, 97*, 13917–13951. https://doi.org/10.1029/92JB01202

Chevrot, S., Sylvander, M., Diaz, J., Martin, R., Mouthereau, F., Manatschal, G., et al. (2018). The non-cylindrical crustal architecture of the Pyrenees. *Scientific Reports*, *8*, 9591. https://doi.org/10.1038/s41598-018-27889-x

Chevrot, S., Sylvander, M., Diaz, J., Ruiz, M., & Paul, A., The PYROPE Working Group. (2015). The Pyrenean architecture as revealed by teleseismic P-to-S converted waves recorded along two dense transects. *Geophysical Journal International*, *200*, 1094–1105. https://doi.org/10.1093/gji/ggu400

Chevrot, S., Villaseñor, A., Sylvander, M., Benahmed, S., Beucler, E., Cougoulat, G., et al. (2014). High-resolution imaging of the Pyrenees and Massif Central from the data of the PYROPE and IBERARRAY portable array deployments. *Journal of Geophysical Research: Solid Earth*, *119*, 6399–6420. https://doi.org/10.1002/2014JB010953

Choukroune, P., & the ECORS-Pyrenees Team. (1989), The ECORS-Pyrenean deep seismic profile reflection data and the overall structure of the orogenic belt, *Tectonics*, *8*, 23–29, https://doi.org/10.1029/TC008i001p00023

Clariana, P., & García-sansegundo, J. (2009). Variscan structure in the eastern part of the Pallaresa massif, Axial Zone of the Pyrenees (NW Andorra). Tectonic implications. *Bulletin de la Societe Geologique de France*, *180*, 501–511. https://doi.org/10.2113/gssgfbull.180.6.501

Clerc, C., & Lagabrielle, Y. (2014). Thermal control on the modes of crustal thinning leading to mantle exhumation: Insights from the Cretaceous Pyrenean hot paleomargins. *Tectonics*, *33*, 1340–1359. https://doi.org/10.1002/2013TC003471

Clerc, C., Lagabrielle, Y., Neumaier, M., Reynaud, J.-Y., & de Saint Blanquat, M. (2012). Exhumation of subcontinental mantle rocks: Evidence from ultramafic-bearing clastic deposits nearby the Lherz peridotite body, French Pyrenees. *Bulletin de la Société Géologique de France*, *183*, 443–459. https://doi.org/10.2113/gssgfbull.183.5.443

Cochelin, B., Lemirre, B., Denèle, Y., de Saint Blanquat, M., Lahfid, A., & Duchêne, S. (2018). Structural inheritance in the central pyrenees: The variscan to alpine tectonometamorphic evolution of the axial zone. *Journal of the Geological Society*, *175*, 336–351. https://doi.org/10.1144/jgs2017-066

Costa, S., & Maluski, H. (1988). Use of the 40Ar- 39Ar stepwise heating method for dating mylonite zones: An example from the St. Barthélémy massif (Northern Pyrenees, France). *Chemical Geology: Isotope Geoscience Section*, *72*, 127–144. https://doi.org/10.1016/0168-9622(88)90061-9

de Saint Blanquat, M., Bajolet, F., Grand'Homme, A., Proietti, A., Zanti, M., Boutin, A., et al. (2016). Cretaceous mantle exhumation in the central Pyrenees: New constraints from the peridotites in eastern Ariège (North Pyrenean zone, France). *Comptes Rendus Geoscience*, *348*, 268–278, From rifting to mountain building: the Pyrenean Belt. https://doi.org/10.1016/j.crte.2015.12.003

Denèle, Y., Olivier, P., & Gleizes, G. (2008). Progressive deformation of a zone of magma transfer in a transpressional regime: The Variscan Mérens shear zone (Pyrenees, France). *Journal of Structural Geology*, *30*, 1138–1149. https://doi.org/10.1016/j.jsg.2008.05.006

Denèle, Y., Olivier, P., Gleizes, G., & Barbey, P. (2009). Decoupling between the middle and upper crust during transpression-related lateral flow: Variscan evolution of the Aston gneiss dome (Pyrenees, France). *Tectonophysics*, *477*, 244–261. https://doi.org/10.1016/j.tecto.2009.04.033

Deramond, J., Fischer, M., Hossack, J., Labaume, P., Seguret, M., Soula, J. C., et al. (1984). Field guide of conference trip to Pyrenees. *Thrusting and Deformation*.

Deramond, J., Souquet, P., Fondecave-Wallez, M.-J., & Specht, M. (1993). Relationships between thrust tectonics and sequence stratigraphy surfaces in foredeeps: Model and examples from the pyrenees (Cretaceous-Eocene, France, Spain). *Geological Society, London, Special Publications*, *71*, 193–219. https://doi.org/10.1144/GSL.SP.1993.071.01.09

Druguet, E., Alsop, G. I., & Carreras, J. (2009). Coeval brittle and ductile structures associated with extreme deformation partitioning in a multilayer sequence. *Journal of Structural Geology*, *31*, 498–511. https://doi.org/10.1016/j.jsg.2009.03.004

Ducoux, M., Jolivet, L., Gumiaux, C., Baudin, T., Cagnard, F., Masini, E., et al. (2018). Unravelling early orogenic pro-cesses: Constraints from the inverted hyper-extended rift pre-served in the basco-cantabrian belt. *Geophysical Research Abstracts*, *20*: EGU2018-19143.

Dumitru, T. A. (1993). A new computer-automated microscope stage system for fission-track analysis. *Nuclear Tracks and Radiation Measurements*, *21*, 575–580. https://doi.org/10.1016/1359-0189(93)90198-I

Erdős, Z., Huismans, R. S., van der Beek, P., & Thieulot, C. (2014). Extensional inheritance and surface processes as controlling factors of mountain belt structure: Inherited structural control on orogens. *Journal of Geophysical Research: Solid Earth*, *119*, 9042–9061. https://doi.org/10.1002/2014JB011408

Espurt, N., Angrand, P., Teixell, A., Labaume, P., Ford, M., de Saint Blanquat, M., et al. (2019). Crustal-scale balanced cross-section and restorations of the Central Pyrenean belt (Nestes-Cinca transect): Highlighting the structural control of Variscan belt and Permian-Mesozoic rift systems on mountain building. *Tectonophysics*, *764*, 25–45. https://doi.org/10.1016/j.tecto.2019.04.026

Evans, N. G. (1993). *Deformation during the emplacement of the Maladeta granodiorite, Spanish Pyrenees (Ph.D.)*. University of Leeds.

Evans, N. G., Gleizes, G., Leblanc, D., & Bouchez, J.-L. (1997). Hercynian tectonics in the pyrenees: A new view based on structural observations around the Bassie`s granite pluton. *Journal of Structural Geology*, *19*, 195–208. https://doi.org/10.1016/S0191-8141(96)00080-6

Filleaudeau, P.-Y. (2011). *Croissance et dénudation des Pyrénées du Crétacé supérieur au paléogène: Apports de l'analyse de bassin et thermochronométrie détritique*. Université Pierre et Marie Curie, Paris.

Fillon, C., Mouthereau, F., Calassou, S., Pik, R., Bellahsen, N., Gautheron, C., et al., in press. Post-orogenic exhumation in the western pyrenees: Evidence for extension driven by pre-orogenic inheritance. *Journal of the Geological Society*, https://doi-org.accesdistant.sorbonne-universite.fr/10.1144/jgs2020-079

Fitzgerald, P. G., Muñoz, J. A., Coney, P. J., & Baldwin, S. L. (1999). Asymmetric exhumation across the pyrenean orogen: Implications for the tectonic evolution of a collisional orogen. *Earth and Planetary Science Letters*, *173*, 157–170. https://doi.org/10.1016/S0012-821X(99)00225-3

Flowers, R. M., Ketcham, R. A., Shuster, D. L., & Farley, K. A. (2009). Apatite (U–Th)/He thermochronometry using a radiation damage accumulation and annealing model. *Geochimica et Cosmochimica Acta*, *73*, 2347–2365. https://doi.org/10.1016/j.gca.2009.01.015

Gallagher, K. (2012). Transdimensional inverse thermal history modeling for quantitative thermochronology: Transdimensional inverse thermal history. *Journal of Geophysical Research*, *117*. https://doi.org/10.1029/2011JB008825

Gallagher, K., Charvin, K., Nielsen, S., Sambridge, M., & Stephenson, J. (2009). Markov chain Monte Carlo (MCMC) sampling methods to determine optimal models, model resolution and model choice for Earth Science problems. *Marine and Petroleum Geology, Thematic Set on Basin Modeling Perspectives*, *26*, 525–535. https://doi.org/10.1016/j.marpetgeo.2009.01.003

García-Sansegundo, J., & Poblet, J. (1997). Variscan granites of the pyrenees revisited: Their role as syntectonic markers of the orogen: Comment to Gleizes et al, 1997. *Terra Nova*, *9*, 144–147.

Garver, J. I., & Kamp, P. J. J. (2002). Integration of zircon color and zircon fission-track zonation patterns in orogenic belts: Application to the southern Alps, New Zealand. *Tectonophysics, Low Temperature Thermochronology: From Tectonics to Landscape Evolution*, *349*, 203–219. https://doi.org/10.1016/S0040-1951(02)00054-9

Garwin, L. J. (1985). *Fission-track dating and tectonics in the eastern Pyrenees (Ph.D. Thesis)*. Cambridge University, Cambridge, United Kingdom.

Gautheron, C., Djimbi, D. M., Roques, J., Balout, H., Ketcham, R. A., Simoni, E., et al. (2020). A multi-method, multi-scale theoretical study of He and Ne diffusion in zircon. *Geochimica et Cosmochimica Acta*, *268*, 348–367. https://doi.org/10.1016/j.gca.2019.10.007

Gautheron, C., Tassan-Got, L., Barbarand, J., & Pagel, M. (2009). Effect of alpha-damage annealing on apatite (U–Th)/He thermochronology. *Chemical Geology*, *266*, 157–170. https://doi.org/10.1016/j.chemgeo.2009.06.001

Gibson, M., Sinclair, H. D., Lynn, G. J., & Stuart, F. M. (2007). Late- to post-orogenic exhumation of the Central Pyrenees revealed through combined thermochronological data and modelling. *Basin Research*, *19*, 323–334. https://doi.org/10.1111/j.1365-2117.2007.00333.x

Girault, J. B., Bellahsen, N., Boutoux, A., Rosenberg, C. L., Nanni, U., Verlaguet, A., et al. (2020). The 3-D thermal structure of the helvetic nappes of the European Alps: Implications for collisional processes. *Tectonics*, *39*. https://doi.org/10.1029/2018TC005334

Gleadow, A. J. W., Hurford, A. J., & Quaife, R. D. (1976). Fission track dating of zircon: Improved etching techniques. *Earth and Planetary Science Letters*, *33*, 273–276. https://doi.org/10.1016/0012-821X(76)90235-1

Gleizes, G., Crevon, G., Asrat, A., & Barbey, P. (2006). Structure, age and mode of emplacement of the hercynian bordères-louron pluton (central pyrenees, France). *International Journal of Earth Sciences*, *95*, 1039–1052. https://doi.org/10.1007/s00531-006-0088-4

Gleizes, G., Leblanc, D., Santana, V., Olivier, P., & Bouchez, J. L. (1998). Sigmoidal structures featuring dextral shear during emplacement of the Hercynian granite complex of Cauterets–Panticosa (Pyrenees). *Journal of Structural Geology*, *20*, 1229–1245. https://doi.org/10.1016/S0191-8141(98)00060-1

Golberg, J. M., & Leyreloup, A. F. (1990). High temperature-low pressure Cretaceous metamorphism related to crustal thinning (Eastern North Pyrenean Zone, France). *Contributions to Mineralogy and Petrology*, *104*, 194–207. https://doi.org/10.1007/BF00306443

Grool, A. R., Ford, M., Vergés, J., Huismans, R. S., Christophoul, F., & Dielforder, A. (2018). Insights into the crustal-scale dynamics of a doubly vergent orogen from a quantitative analysis of its forelands: A case study of the eastern pyrenees. *Tectonics*, *37*, 450–476. https://doi.org/10.1002/2017TC004731

Guenthner, W. R., Reiners, P. W., Ketcham, R. A., Nasdala, L., & Giester, G. (2013). Helium diffusion in natural zircon: Radiation damage, anisotropy, and the interpretation of zircon (U-Th)/He thermochronology. *American Journal of Science*, *313*, 145–198. https://doi.org/10.2475/03.2013.01

Hurford, A. J., & Green, P. F. (1983). The zeta age calibration of fission-track dating. *Chemical Geology*, *41*, 285–317. https://doi.org/10.1016/S0009-2541(83)80026-6

Huyghe, D., Mouthereau, F., & Emmanuel, L. (2012). Oxygen isotopes of marine mollusc shells record Eocene elevation change in the Pyrenees. *Earth and Planetary Science Letters*, *345–348*, 131–141. https://doi.org/10.1016/j.epsl.2012.06.035

Jammes, S., Manatschal, G., Lavier, L., & Masini, E. (2009). Tectonosedimentary evolution related to extreme crustal thinning ahead of a propagating ocean: Example of the western pyrenees: Extreme crustal thinning IN the pyrenees. *Tectonics*, *28*. https://doi.org/10.1029/2008TC002406

Jolivet, M., Labaume, P., Monié, P., Brunel, M., Arnaud, N., & Campani, M. (2007). Thermochronology constraints for the propagation sequence of the South pyrenean basement thrust system (France-Spain): Propagation OF the South pyrenean prism. *Tectonics*, *26*, n/a-n/a. https://doi.org/10.1029/2006TC002080

Jourdon, A., Le Pourhiet, L., Mouthereau, F., & Masini, E. (2019). Role of rift maturity on the architecture and shortening distribution in mountain belts. *Earth and Planetary Science Letters*, *512*, 89–99. https://doi.org/10.1016/j.epsl.2019.01.057

Ketcham, R. A., Carter, A., Donelick, R. A., Barbarand, J., & Hurford, A. J. (2007). Improved modeling of fission-track annealing in apatite. *American Mineralogist*, *92*, 799–810. https://doi.org/10.2138/am.2007.2281

Ketcham, R. A., Gautheron, C., & Tassan-Got, L. (2011). Accounting for long alpha-particle stopping distances in (U–Th–Sm)/He geochronology: Refinement of the baseline case. *Geochimica et Cosmochimica Acta*, *75*, 7779–7791. https://doi.org/10.1016/j.gca.2011.10.011

Ketcham, R. A., Guenthner, W. R., & Reiners, P. W. (2013). Geometric analysis of radiation damage connectivity in zircon, and its implications for helium diffusion. *American Mineralogist*, *98*, 350–360. https://doi.org/10.2138/am.2013.4249

Labaume, P., Séguret, M., & Seyve, C. (1985). Evolution of a turbiditic foreland basin and analogy with an accretionary prism: Example of the Eocene South-Pyrenean Basin. *Tectonics*, *4*, 661–685. https://doi.org/10.1029/TC004i007p00661

Lagabrielle, Y., & Bodinier, J.-L. (2008). Submarine reworking of exhumed subcontinental mantle rocks: Field evidence from the lherz peridotites, French pyrenees. *Terra Nova*, *20*, 11–21. https://doi.org/10.1111/j.1365-3121.2007.00781.x

Lagabrielle, Y., Labaume, P., & de Saint Blanquat, M. (2010). Mantle exhumation, crustal denudation, and gravity tectonics during cretaceous rifting in the pyrenean realm (SW Europe): Insights from the geological setting of the lherzolite bodies: Pyrenean lherzolites, gravity tectonics. *Tectonics*, *29*, n/a-n/a. https://doi.org/10.1029/2009TC002588

Laumonier, B. (2010). Polymétamorphisme et évolution crustale dans les Pyrénées orientales pendant l'orogenèse varisque au Carbonifère supérieur. *Sull. Soc. géol. Fr.*, *181*, 411–428.

Laumonier, B., Barbey, P., Denèle, Y., Olivier, P., & Paquette, J.-L. (2014). Réconcilier les données stratigraphiques, radiométriques, plutoniques, volcaniques et structurales au Pennsylvanien supérieur (Stéphanien - autunien p.p.) dans l'Est des Pyrénées hercyniennes (France, Espagne). *Rev. Géol. pyrén.*, *1*, 10.

Masini, E., Manatschal, G., Tugend, J., Mohn, G., & Flament, J.-M. (2014). The tectono-sedimentary evolution of a hyper-extended rift basin: The example of the arzacq–mauléon rift system (western pyrenees, SW France). *International Journal of Earth Sciences*, *103*, 1569–1596. https://doi.org/10.1007/s00531-014-1023-8

Maurel, O. (2003). L'exhumation de la Zone Axiale des Pyrénées orientales: Une approche thermo-chronologique multi-méthodes du rôle des failles. *Université Montpellier II - Sciences et Techniques du Languedoc*.

Maurel, O., Monié, P., Pik, R., Arnaud, N., Brunel, M., & Jolivet, M. (2008). The meso-cenozoic thermo-tectonic evolution of the eastern pyrenees: An 40Ar/39Ar fission track and (U–Th)/He thermochronological study of the canigou and mont-louis massifs. *International Journal of Earth Sciences*, *97*, 565–584. https://doi.org/10.1007/s00531-007-0179-x

Maurel, O., Monié, P., Respaut, J. P., Leyreloup, A. F., & Maluski, H. (2003). Pre-metamorphic 40Ar/39Ar and U–Pb ages in HP metagranitoids from the Hercynian belt (France). *Chemical Geology*, *193*, 195–214. https://doi.org/10.1016/S0009-2541(02)00351-0

McCaig, A. (1986). Thick- and thin-skinned tectonics in the Pyrenees. *Tectonophysics*, *129*, 319–342. https://doi.org/10.1016/0040-1951(86)90259-3

McCaig, A. M., & Miller, J. A. (1986). 40Ar-39Ar age of mylonites along the Merens Fault, central Pyrenees. *Tectonophysics*, *129*, 149–172. https://doi.org/10.1016/0040-1951(86)90250-7

Meigs, A. J., & Burbank, D. W. (1997). Growth of the south pyrenean orogenic wedge. *Tectonics*, *16*, 239–258. https://doi.org/10.1029/96TC03641

Meigs, A. J., Vergés, J., & Burbank, D. W. (1996). Ten-million-year history of a thrust sheet. *The Geological Society of America Bulletin*, *108*, 1608–1625. https://doi.org/10.1130/0016-7606(1996)108<1608:TMYHOA>2.3.CO;2

Metcalf, J. R., Fitzgerald, P. G., Baldwin, S. L., & Muñoz, J.-A. (2009). Thermochronology of a convergent orogen: Constraints on the timing of thrust faulting and subsequent exhumation of the Maladeta pluton in the central pyrenean axial zone. *Earth and Planetary Science Letters*, *287*, 488–503. https://doi.org/10.1016/j.epsl.2009.08.036

Mezger, J. E., Schnapperelle, S., & Rölke, C. (2012). Evolution of the Central Pyrenean Mérens fault controlled by near collision of two gneiss domes. *Hallesches Jahrbuch für Geowissenschaften*, *34*, 11–29.

Montigny, R., Azambre, B., Rossy, M., & Thuizat, R. (1986). K-Ar Study of cretaceous magmatism and metamorphism in the pyrenees: Age and length of rotation of the Iiberian Peninsula. Tectonophysics, *The Geological Evolution of the Pyrenees*, *129*, 257–273. https://doi.org/10.1016/0040-1951(86)90255-6

Morris, R. G., Sinclair, H. D., & Yelland, A. J. (1998). Exhumation of the pyrenean orogen: Implications for sediment discharge. *Basin Research*, *10*, 69–85.

Mouthereau, F., Filleaudeau, P.-Y., Vacherat, A., Pik, R., Lacombe, O., Fellin, M. G., et al. (2014). Placing limits to shortening evolution in the Pyrenees: Role of margin architecture and implications for the Iberia/Europe convergence: Plate convergence in the Pyrenees. *Tectonics*, *33*, 2283–2314. https://doi.org/10.1002/2014TC003663

Muñoz, J. A. (1992). Evolution of a continental collision belt: ECORS-Pyrenees crustal balanced cross-section, in: McClay, K. R. (Ed.), *Thrust tectonics*. Springer Netherlands, Dordrecht, pp. 235–246. https://doi.org/10.1007/978-94-011-3066-0_21

Naylor, M., & Sinclair, H. D. (2008). Pro- vs. retro-foreland basins: Pro- vs. retro-foreland basins. *Basin Research*, *20*, 285–303. https://doi.org/10.1111/j.1365-2117.2008.00366.x

Olivet, J. (1996). Kinematics of the iberian plate. *Bulletin des Centres de Recherches Exploration-Production Elf-Aquitaine*, *20*, 131–195.

Olivier, P., Gleizes, G., Paquette, J.-L., & Muñoz Sáez, C. (2008). Structure and U–Pb dating of the saint-arnac pluton and the ansignan charnockite (agly massif): A cross-section from the upper to the middle crust of the variscan eastern pyrenees. *Journal of the Geological Society*, *165*, 141–152. https://doi.org/10.1144/0016-76492006-185

Paquette, J.-L., Gleizes, G., Leblanc, D., & Bouchez, J. L. (1997). Le granite de Bassiés (Pyrénées): Un pluton syntectonique d'âge westphalien. Géochronologie U–Pb sur zircons. *Comptes Rendus de l'Academie des Sciences - Series IIA: Earth and Planetary Science*, *324*, 387–392.

Passchier, C. W. (1984). Mylonite-dominated footwall geometry in a shear zone, central Pyrenees. *Geological Magazine*, *121*, 429–436. https://doi.org/10.1017/S0016756800029964

Puigdefàbregas, C., & Souquet, P. (1986). Tecto-sedimentary cycles and depositional sequences of the mesozoic and tertiary from the pyrenees. *Tectonophysics*, *129*, 173–203. https://doi.org/10.1016/0040-1951(86)90251-9

Rahl, J. M., Haines, S. H., & van der Pluijm, B. A. (2011). Links between orogenic wedge deformation and erosional exhumation: Evidence from illite age analysis of fault rock and detrital thermochronology of syn-tectonic conglomerates in the Spanish Pyrenees. *Earth and Planetary Science Letters*, *307*, 180–190. https://doi.org/10.1016/j.epsl.2011.04.036

Rahn, M. K., Brandon, M. T., Batt, G. E., & Garver, J. I. (2004). A zero-damage model for fission-track annealing in zircon. *American Mineralogist*, *89*, 473–484. https://doi.org/10.2138/am-2004-0401

Respaut, J. P., Lancelot, J. P., & Lancelot, J. R. (1983). Datation de la mise en place synmétamorphe de la charnockite d'Ansignan (massif de l'Agly) par la méthode U/Pb sur zircons et monazites. *Neues Jahrbuch für Mineralogie - Abhandlungen*, 21–34.
Roberts, M. P., Pin, C., Clemens, J. D., & Paquette, J.-L. (2000). Petrogenesis of mafic to felsic plutonic rock associations: The calc-alkaline quérigut complex, French pyrenees. *Journal of Petrology*, *41*, 809–844. https://doi.org/10.1093/petrology/41.6.809
Rosenbaum, G., Lister, G. S., & Duboz, C. (2002). Relative motions of africa, Iberia and Europe during alpine orogeny. *Tectonophysics*, *359*, 117–129. https://doi.org/10.1016/S0040-1951(02)00442-0
Roure, F., Choukroune, P., Berastegui, X., Muñoz, J. A., Villien, A., Matheron, P., et al. (1989). Ecors deep seismic data and balanced cross sections: Geometric constraints on the evolution of the Pyrenees. *Tectonics*, *8*, 41–50. https://doi.org/10.1029/TC008i001p00041
Saspiturry, N., Razin, P., Baudin, T., Serrano, O., Issautier, B., Lasseur, E., et al. (2019). Symmetry vs. asymmetry of a hyper-thinned rift: Example of the mauléon basin (western pyrenees, France). *Marine and Petroleum Geology*, *104*, 86–105. https://doi.org/10.1016/j.marpetgeo.2019.03.031
Schärer, U., de Parseval, P., Polvé, M., & de Saint Blanquat, M. (1999). Formation of the Trimouns talc-chlorite deposit (Pyrenees) from persistent hydrothermal activity between 112 and 97 Ma, *Terra Nova*, *11*(1), 30–37, https://doi.org/10.1046/j.1365-3121.1999.00224.x
Schettino, A., & Turco, E. (2011). Tectonic history of the western Tethys since the late triassic. *The Geological Society of America Bulletin*, *123*, 89–105. https://doi.org/10.1130/B30064.1
Seguret, M. (1972). *Etude tectonique des nappes de series décollées de la partie centrale du versant sud des Pyrénées. Caractère synsédimentaire, rôle de la compression et de la gravité*. 2, Montpellier: Université des Sciences et Technique du Languedoc. http://www.sudoc.fr/012768294
Sinclair, H. D. (2005). Asymmetric growth of the Pyrenees revealed through measurement and modeling of orogenic fluxes. *American Journal of Science*, *305*, 369–406. https://doi.org/10.2475/ajs.305.5.369
Soler, D., Teixell, A., & García-Sansegundo, J. (1998). Eastward displacement reduction of the Gavarnie thrust and implications for South Pyrenean thrusting. *Comptes Rendus de l'Academie des Sciences - Series IIA: Earth and Planetary Science*, *327*, 699–704. https://doi.org/10.1016/S1251-8050(99)80028-7
Srivastava, S. P., Roest, W. R., Kovacs, L. C., Oakey, G., Lévesque, S., Verhoef, J., et al. (1990). Motion of Iberia since the late jurassic: Results from detailed aeromagnetic measurements in the newfoundland basin. *Tectonophysics, Alpine Evolution of Iberia and its Continental Margins*, *184*, 229–260. https://doi.org/10.1016/0040-1951(90)90442-B
Tagami, T., Galbraith, R. F., Yamada, R., & Laslett, G. M. (1998). Revised annealing kinetics of fission tracks in zircon and geological implications, In: van den Haute, P., & de Corte, F. (Eds.), *Advances in fission-track geochronology: A selection of papers presented at the international workshop on fission-track dating, ghent, Belgium, 1996, solid earth sciences library*. Springer Netherlands, Dordrecht, pp. 99–112. https://doi.org/10.1007/978-94-015-9133-1_8
Teixell, A. (1996). The ansó transect of the southern pyrenees: Basement and cover thrust geometries. *Journal of the Geological Society*, *153*, 301–310. https://doi.org/10.1144/gsjgs.153.2.0301
Teixell, A. (1998). Crustal structure and orogenic material budget in the west central Pyrenees. *Tectonics*, *17*, 395–406. https://doi.org/10.1029/98TC00561
Teixell, A., Labaume, P., Ayarza, P., Espurt, N., de Saint Blanquat, M., & Lagabrielle, Y. (2018). Crustal structure and evolution of the pyrenean-cantabrian belt: A review and new interpretations from recent concepts and data. *Tectonophysics*, *724–725*, 146–170. https://doi.org/10.1016/j.tecto.2018.01.009
Ternet, Y., Majeste-Menjoulas, J., Canérot, J., Baudin, T., Cocherie, C., Guerrot, C., et al. (2004). *Notice explicative de la feuille Laruns-Somport* (p. 192).
Ternois, S., Odlum, M., Ford, M., Pik, R., Stockli, D., Tibari, B., et al. (2019). Thermochronological evidence of early orogenesis, eastern pyrenees, France. *Tectonics*, *38*, 1308–1336. https://doi.org/10.1029/2018TC005254
Thinon, I., Fidalgo-González, L., Réhault, J.-P., & Olivet, J.-L. (2001). Déformations pyrénéennes dans le golfe de Gascogne. *Comptes Rendus de l'Academie des Sciences - Series IIA: Earth and Planetary Science*, *332*, 561–568. https://doi.org/10.1016/S1251-8050(01)01576-2
Tibari, B., Vacherat, A., Stab, M., Pik, R., Yeghicheyan, D., & Hild, P. (2016). An alternative protocol for single zircon dissolution with application to (U-Th-Sm)/He thermochronometry. *Geostandards and Geoanalytical Research*, *40*, 365–375. https://doi.org/10.1111/j.1751-908X.2016.00375.x
Tugend, J., Manatschal, G., & Kusznir, N. J. (2015). Spatial and temporal evolution of hyperextended rift systems: Implication for the nature, kinematics, and timing of the Iberian-European plate boundary. *Geology*, *43*, 15–18. https://doi.org/10.1130/G36072.1
Vacherat, A., Mouthereau, F., Pik, R., Bellahsen, N., Gautheron, C., Bernet, M., et al. (2016). Rift-to-collision transition recorded by tectonothermal evolution of the northern Pyrenees. *Tectonics*, *35*, 907–933. https://doi.org/10.1002/2015TC004016
Vacherat, A., Mouthereau, F., Pik, R., Bernet, M., Gautheron, C., Masini, E., et al. (2014). Thermal imprint of rift-related processes in orogens as recorded in the Pyrenees. *Earth and Planetary Science Letters*, *408*, 296–306. https://doi.org/10.1016/j.epsl.2014.10.014
Vacherat, A., Mouthereau, F., Pik, R., Huyghe, D., Paquette, J.-L., Christophoul, F., et al. (2017). Rift-to-collision sediment routing in the pyrenees: A synthesis from sedimentological, geochronological and kinematic constraints. *Earth-Science Reviews*, *172*, 43–74. https://doi.org/10.1016/j.earscirev.2017.07.004
Vauchez, A., Clerc, C., Bestani, L., Lagabrielle, Y., Chauvet, A., Lahfid, A., et al. (2013). Preorogenic exhumation of the north pyrenean agly massif (eastern pyrenees-France): Exhumation OF the North pyrenean massifs. *Tectonics*, *32*, 95–106. https://doi.org/10.1002/tect.20015
Vergés, J., Millán, H., Roca, E., Muñoz, J. A., Marzo, M., Cirés, J., et al. (1995). Eastern pyrenees and related foreland basins: Pre-, syn- and post-collisional crustal-scale cross-sections. *Marine and Petroleum Geology, Integrated Basin Studies*, *12*, 903–915. https://doi.org/10.1016/0264-8172(95)98854-X
Vermeesch, P. (2009). RadialPlotter: A java application for fission track, luminescence and other radial plots. *Radiation Measurements*, *44*, 409–410. https://doi.org/10.1016/j.radmeas.2009.05.003
Vielzeuf, D., & Kornprobst, J. (1984). Crustal splitting and the emplacement of Pyrenean lherzolites and granulites. *Earth and Planetary Science Letters*, *67*, 87–96. https://doi.org/10.1016/0012-821X(84)90041-4
Vissers, R. L. M. (1992). Variscan extension in the pyrenees. *Tectonics*, *11*, 1369–1384. https://doi.org/10.1029/92TC00823
Wayne, D. M., & McCaig, A. M. (1998). Dating fluid flow in shear zones: Rb-Sr and U-Pb studies of syntectonic veins in the néouvielle massif, pyrenees. *Geological Society, London, Special Publications*, *144*, 129–135. https://doi.org/10.1144/GSL.SP.1998.144.01.09
Whitchurch, A. L., Carter, A., Sinclair, H. D., Duller, R. A., Whittaker, A. C., & Allen, P. A. (2011). Sediment routing system evolution within a diachronously uplifting orogen: Insights from detrital zircon thermochronological analyses from the South-Central Pyrenees. *American Journal of Science*, *311*, 442–482. https://doi.org/10.2475/05.2011.03
Yamada, R., Murakami, M., & Tagami, T. (2007). Statistical modelling of annealing kinetics of fission tracks in zircon; Reassessment of laboratory experiments. *Chemical Geology*, *236*, 75–91. https://doi.org/10.1016/j.chemgeo.2006.09.002
Yelland, J. (1991). *Thermo-Tectonics of the Pyrenees and provenance from fission-track studies*. Birbeck College, Univ. of London, London.